

Geometric Confinement Reveals Scale-Free Velocity Correlations in Epithelial Cell Monolayer

Guillaume Duprez^{*1}, Mélina Durande^{*2}, François Graner², Hélène Delanoë-Ayari^{†1}

¹Université Claude Bernard - Lyon 1, CNRS, ILM, UMR5306, F-69100 Villeurbanne, France.

²Université Paris Cité, CNRS, MSC, UMR7057, F-75006 Paris, France.

Abstract

Collective cell flows are a hallmark of tissue dynamics in development, wound healing, and various diseases. Here, we perform experiments on epithelial MDCK cell monolayers, over tens of hours without jamming, on millimeter-scale micropatterned substrates with or without free front (a strip or a closed racetrack). During maturation in time, domains and long-range correlations of the velocity field appear. Enstrophy increases (along with kinetic energy) during 5 hours, then passes through a maximum and decreases. Spatial velocity correlations are scale-free, following a power law, which challenges the notion of a single intrinsic correlation length. It suggests that the monolayer behaves as a critical-like system where information is transmitted across its entire size, a feature consistent with models of active solids capable of long-range stress propagation. The spatial correlation exponent significantly evolves with time, probably reflecting the monolayer maturation. The size, shape, topology and rigidity of patterned substrate influence the organization of flows and mechanical fields. Spontaneous collective motions are stronger on soft than on hard substrate. The presence of a free front accumulates vimentin on a much larger length scale than a fixed boundary ($65 \pm 4 \mu\text{m}$ vs $3.2 \pm 0.7 \mu\text{m}$), possibly revealing an underlying polarizing cue on the cell velocity field.

1 Introduction

Collective cellular movement plays a crucial role in various biological processes, including tissue development, wound healing, and cancer metastasis [1, 2]. It involves coordinated interactions between cells, enabling them to move as a cohesive group. This behavior is influenced by a combination of biochemical signals, mechanical forces, and environmental cues, creating a complex interplay that governs their collective dynamics [3–5].

1.1 State of the art

Experiments on confluent epithelial monolayers since two decades [6] have probed *in vitro* migration by culturing cells on solid substrates patterned to create various geometries delineated by non-adhesive regions, for instance within a strip [7], within an annulus [8, 9], within a circle [10, 11], or around it [12]. If one of the non-adhesive boundaries is mobile, removing it creates a front for the cell layer and a free space in which

^{*}Authors contributed equally to this work.

[†]Corresponding author: helene.ayari@univ-lyon1.fr

migration becomes suddenly possible, as in the so-called “wound healing assay” where cells migrate to invade or expand from rectangular [6, 13] or circular [14, 15] regions. Such biophysical experiments established several results that deepen our understanding of collective migration.

Cells near an unfilled space exert pulling forces towards it regardless of their migration direction [12], and the presence of a free front modulates both cell self-propulsion and alignment strength, favoring flowing states that propagate into the monolayer bulk [16]. Fronts may undergo fingering instabilities where lateral heterogeneities penetrate the epithelium over distances comparable to finger lengths [17, 18]. Cells at finger tips extend protrusions with distinct morphologies characterized by large, highly active lamellipodia, their number and direction tuned by local front curvature whether spontaneous or experimentally imposed [15].

Further behind the front, cells contribute traction forces on the substrate with some actively driving motion and others acting as mechanical resistors [3, 19]. The balance of traction forces and substrate friction is captured by the epithelialization coefficient, distinguishing bulk- versus boundary-dominated behaviors [14]. Competition between traction and cell-cell interaction forces can lead to active wetting transitions, where tissues either spread or retract based on their size [20]. Cell-cell interactions also stimulate motility and regulate transitions between mesenchymal and epithelial behaviors, facilitating the onset of collective migration [7, 21–23].

Velocity and density variations within cell cohorts contribute to continuum mechanical descriptions, where velocity typically decreases with increasing cell density both in strips [24] and circular corrals [10]. Boundary conditions allowing sufficient space lead to large-scale solid-body rotational movements (“swirls” or “vortices”) with uniform angular velocity over tens of cell lengths, as observed across various geometries including strips, circles, and annuli [7, 8, 10, 25].

From a theoretical perspective, collective migration of epithelial monolayers is well-suited to continuum mechanics descriptions via coarse-graining from the individual cell scale to the cohort scale [26]. The cell sheet exhibits properties akin to a glass [27] or a liquid crystal [28]. Internally, cell-cell interaction forces are represented by a stress tensor, either extensile or contractile in nature [29], while traction and friction forces between cells and the substrate form external forces per unit area. These external forces balance the divergence of the internal stress, multiplied by tissue thickness, linking internal and external mechanical cues [30].

1.2 Current approach

Here, we take advantage of MDCK II epithelial cells being a well established model of confluent cell monolayer migration, and we build on the existing experimental protocols (recalled in details in Section S1). We want to study and disentangle the effects on collective cell movement of pattern size, shape, topology and rigidity. More precisely, we want to focus on the correlation between cell movements, not only to understand how far cells coordinate within the bulk, but also to detect how boundaries (whether free or confining) propagate their influence towards the bulk. These multi-scale questions require large systems, long durations and strong statistics.

Two of our papers have introduced a method for that purpose, applied to cells migrating within a cell-adhesive strip which was either bare [24] or with the inclusion of a circular obstacle (i.e. a non-adhesive circle) [31]. The duration of anterior experiments reported in the literature had been limited to a few hours by cell jamming, due to the increase in cell density. We have added the mytomicin drug before beginning the experiment (see Section S1.1.1) to decrease the cell division rate by at least a factor of five. This, combined with the cell density decrease due to the monolayer spreading, has prevented the cell density to increase beyond the jamming point. We have imaged the monolayer for more than a day, during which time the cells have migrated over several millimeters. With an interframe time of 5 min and a cell size of order of 10 μm , our collective migration movies have covered more than two decades both in time and in space. This has enabled us to obtain with unprecedented signal-to-noise ratio several results, including the observation of twelve successive velocity and density waves [24], and the determination of the monolayer visco-elastic time [31].

In the present paper, we analyze images from sub-cellular scale to hundred-cells scale while comparing two different pattern geometries, both having a large size and a non-trivial topology. One is the already used [31] strip made favorable to cell adhesion thanks to fibronectin with the inclusion of a non-adherent circular obstacle (Section 2), within which cells migrate with a free front after removal of a mobile boundary (which,

for technical reasons, requires a hard substrate); we perform 16 measurements. The other is a racetrack [32] without free front (Section 3), with circular obstacles too, with variable dimensions (see Supp. Movies 1-2) or chiral V-shaped design obstacles (see Supp. Movie 3); we performed 66 measurements, on 48 hard substrates (both for convenience and to legitimate comparisons with the strip), see Table S1 and Fig. S1. In addition, we realize racetracks on soft substrate to measure cell traction forces through the deformation they induce in the substrate and perform 4 measurements (2 with $W = 1000 \mu\text{m}$ and 2 with $W = 600 \mu\text{m}$). Finally, we focus on spatial and temporal correlations (Section 4).

Overall, the three main novel features of the present study are: (i) analysis of velocity correlations on larger time- and length-scales than in the literature; (ii) comparison between open geometry with free front, and closed periodic geometry, performed in similar experimental conditions; (iii) correlation with vimentin at boundaries.

2 Strip, with free front

The strip geometry (Fig. 1) is as previously described [31]. Briefly, a rectangular strip, of length $L \approx 3000 \mu\text{m}$ and width $W = 1000 \pm 10 \mu\text{m}$ is made adhesive over all its length except that, in its center, a circular region of radius $130 \pm 10 \mu\text{m}$ is made non-adhesive (the “obstacle”). A mobile boundary is placed in the middle of the strip. MDCK cells are then seeded in the accessible adhesive zone (left part of the strip) and grow until confluence. At $t = 0$, the mobile boundary is removed. This manipulation involves some delay before the movie can be recorded, and requires a hard substrate to preserve the cell monolayer and substrate integrities (here the PDMS substrate rigidity modulus is 1 to 2 MPa, much too large for cells to deform it). By active migration, cells at the free front spread towards the newly accessible adhesive zone (right part of the strip) and the collective movement begins. Since cells conserve their volume, their height steadily decreases with time until it plateaus.

2.1 Velocity field is spatially graded

The presence of a free boundary induces a directional flow with a gradient in both velocity and density (number of cells per unit surface). We measure cell velocities using the Kanade-Lucas-Tomasi algorithm [33, 34] which tracks on successive images landmarks of high local intensity gradient (Section S1.4.1). The resulting velocity field Fig. 2a) displays a high inter-experiments variability, mostly due to variations in initial cell density. We first normalize each velocity field by dividing it by its median velocity measured in the region of interest (ROI, i.e. field of view centered around the obstacle, Fig. 2b). This adimensioned velocity field is noted $\vec{v}(x, y, t)$, where x is the axis parallel to the strip length L and y across the strip width W . It has a reduced variability, and if we average it both over time (here, over 8 hours) and across different experiments we retrieve a smooth field (Fig. 2b).

Whether averaged over time, over space or over experiment repeats, the flow has a non-zero average parallel to the strip. To improve the signal-to-noise ratio, we perform a multiple averaging of the x -component of $\vec{v}(x, y, t)$, as follows. We first average it over y . This defines a one-dimensional velocity field $\bar{V}(x, t) = \int_{y=0}^{y=W} v_x(x, y, t) dy / W$. We then perform the average of $\bar{V}(x, t)$ over time, then ensemble average it over experiments. As expected [24], it exhibits a well-defined spatial gradient characteristic of the migration with a free front. The final signal-to-noise ratio reaches ~ 10 despite a high standard deviation (~ 0.2 in adimensioned units), see Fig. 2c.

2.2 Obstacle influence range is anisotropic

The obstacle locally perturbs the flow direction, and this perturbation too has a non-zero average whether over time, over space or over experiment repeats. In the past, the presence of an obstacle has helped us probe the cell monolayer visco-elastic nature [31] and has been shown to be a discriminant benchmark between numerical models of active collective motions [35]. Here we take advantage of it to measure the deviation of cell velocity around this non-zero average, either locally around the obstacle, or globally across the whole strip.

To evidence how far the obstacle influences the flow, we subtract the spatial gradient to obtain the relative velocity $\vec{V}^{rel}(x, y, t) = \vec{v}(x, y, t) - \bar{V}(x, t)\vec{x}$ and obtain the velocity field in the (virtual) reference

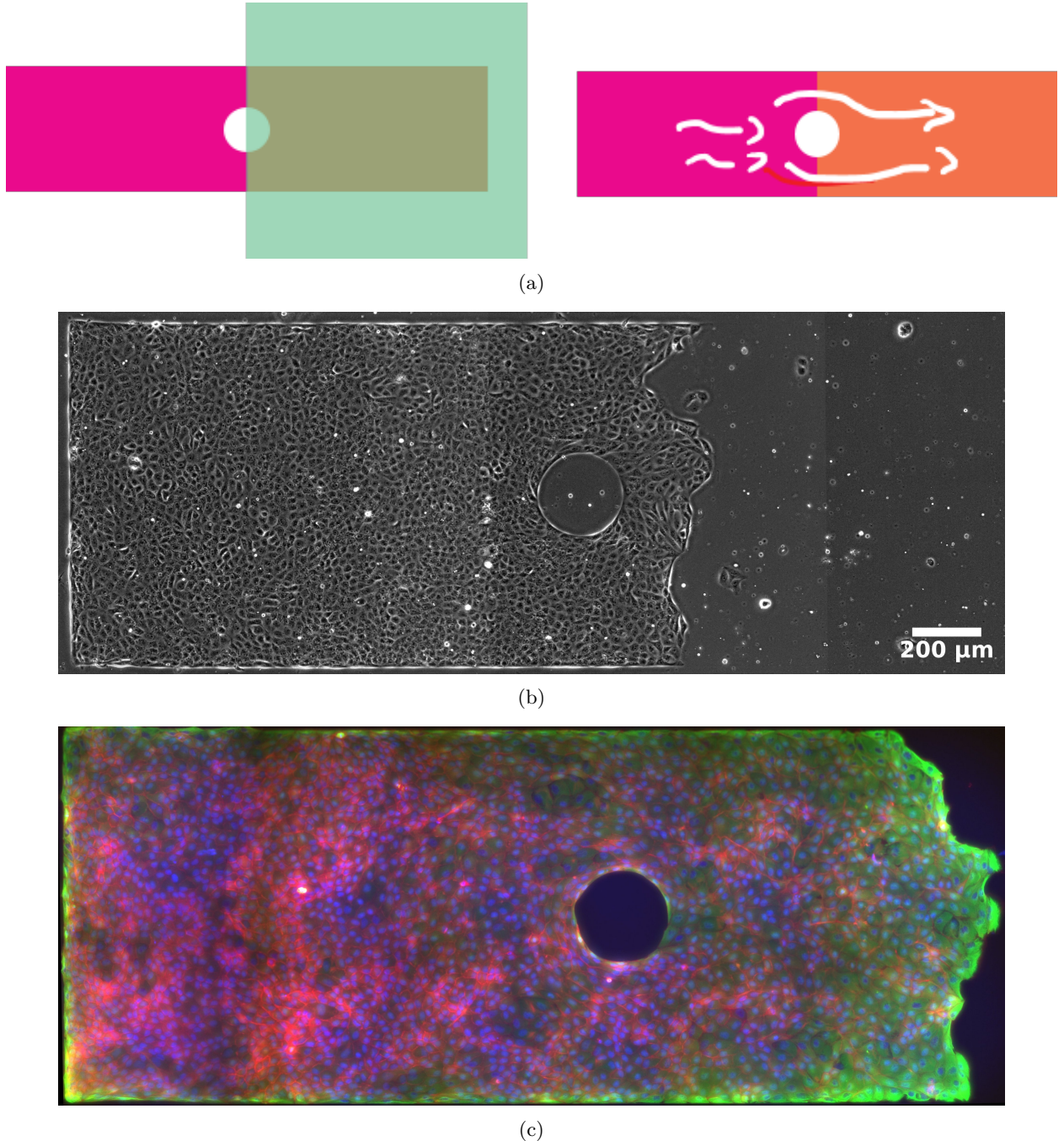


Figure 1: Strip setup. (a) Schematics, with adhesive substrate regions in orange when bare and in pink when covered with cells; left: strip at $t < 0$, i.e., before removal of the mobile non-adhesive boundary; right: at $t > 0$, after removal, white arrows mark directional flow. (b) Beginning of the experiment, live imaging, phase contrast. For legibility, the strip bare parts on the picture right are not shown. (c) 16 h later, fixed image, triple staining: nuclei (blue), actin (red), vimentin (green).

frame of the cells within which the obstacle would be moving. Upstream and downstream, there are arrest points which are very localized ($\sim 1/4$ of the obstacle diameter) and on either lateral sides an acceleration as wide as the strip itself (up to the top and bottom boundaries of Fig. 2d,e). This representation facilitates the comparison with passive incompressible materials, where the upstream and downstream obstacle influence

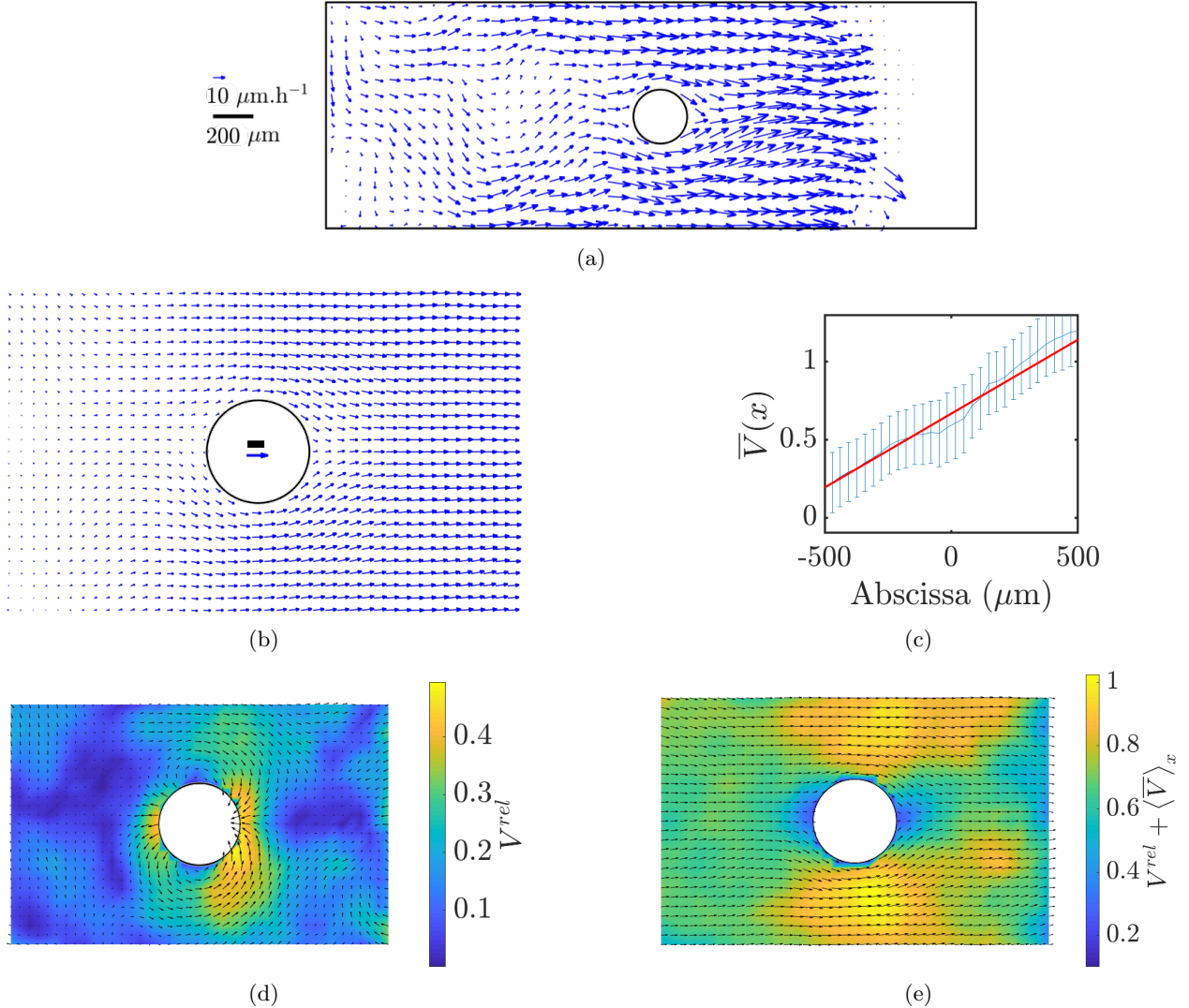


Figure 2: Velocity field in a strip with a circular obstacle. Axis x is parallel to the strip long axis (here horizontal), oriented towards the right. (a) Snapshot of velocity field. (b) Average velocity field $\vec{v}(x, y)$. The “region of interest” (ROI) is the rectangle centered around the obstacle, vertical width W , horizontal length $1.5 W$. For each frame, the velocity field is adimensioned by its median value within this frame. It is then averaged over time t (over 8 h) and over 16 different experiments. Black scale bar: $50 \mu\text{m}$. Blue scale arrow for adimensioned velocity: twice the median velocity. (c) Average of (b) across the strip width of the velocity x -component, $\bar{V}(x)$. Red straight line: linear fit. (d) Relative velocity $\bar{V}^{rel}(x, y) = \vec{v}(x, y) - \bar{V}(x)\vec{x}$, i.e. in the virtual reference frame of the monolayer: same velocity field as in (b) after subtraction of the speed gradient (c). (e) Gradient-less velocity back in the substrate reference frame, i.e. same velocity field as in (d) after addition of the spatial average of velocity.

extends to several obstacle diameters [36], and with active collective movements of particles, where the lateral obstacle influence is much narrower [35].

2.3 Effect of the free front

In free front experiments, mechanical forces mediate intercellular signaling, providing and propagating guidance cues for collective cell migration [37, 38]. Cells can be highly polarized in the direction of the free front, even far from the front itself. Hence the free front boundary condition plays the role of an external

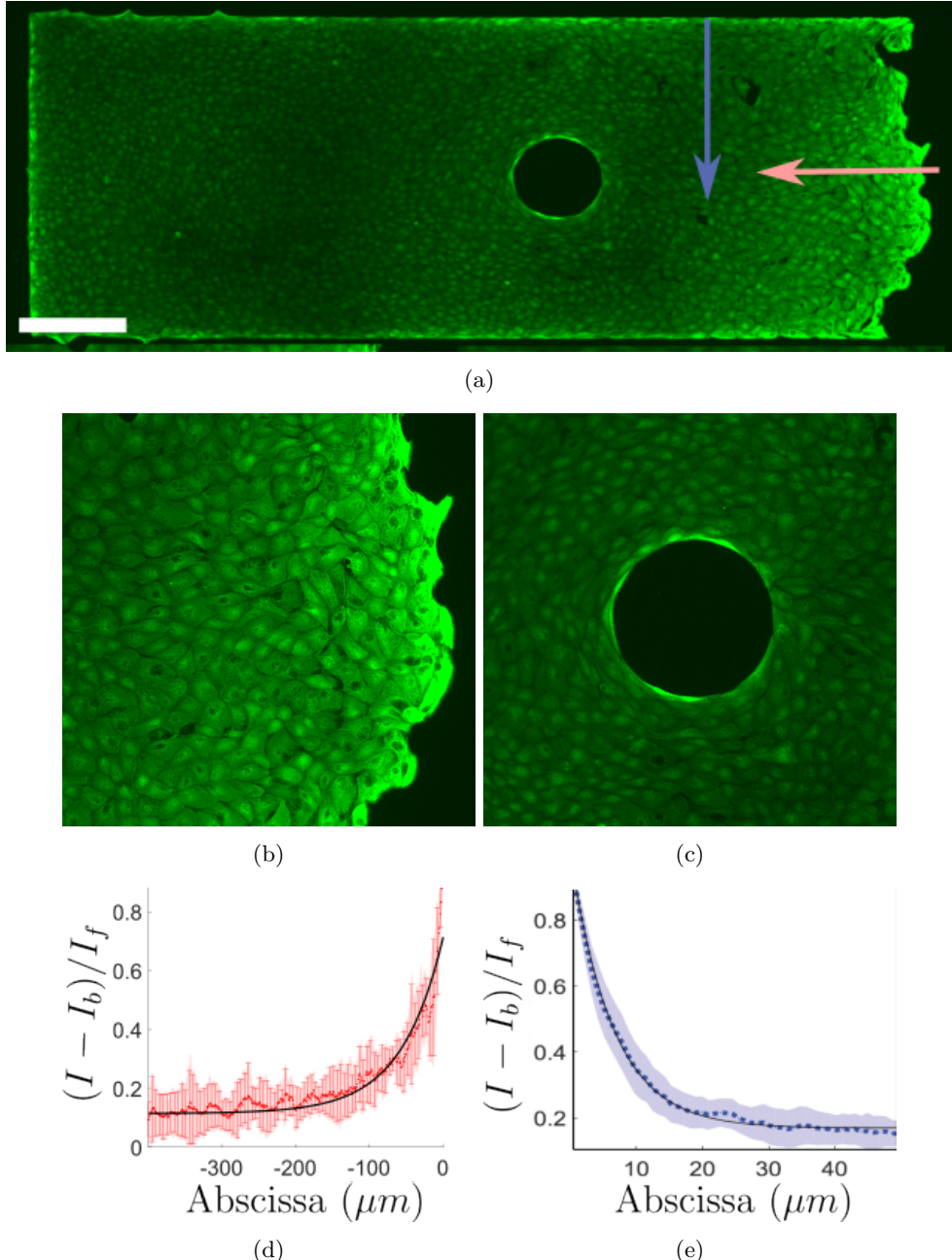


Figure 3: Vimentin in a strip. (a) Global view of vimentin in a strip, showing a brighter staining at boundaries. (b) Zoom on the front. (c) Zoom on the obstacle. (d) Fluorescence intensity vs distance from the free boundary, measured along the horizontal red arrow in (a). (e) Fluorescence intensity vs distance from the confining boundary, measured along the vertical blue arrow in (a).

polarization cue. We do not observe any actin cable near the boundaries (Fig. 1c). In order to test how cells might detect their distance from this external cue, we stained them for vimentin, an intermediate filament. Vimentin plays a prominent role in force generation [39, 40] and is also a marker of the epithelial-to-mesenchymal transition, which is important in cancer and wound healing. Vimentin is overexpressed when cells begin to migrate, in particular near the free front [41].

Here we observe that vimentin marks in fact all boundaries, whether confining or free (Fig. 3a-c). Its expression level is spatially graded at the vicinity of the boundaries (Fig. 3b,c). The intensity curve vs

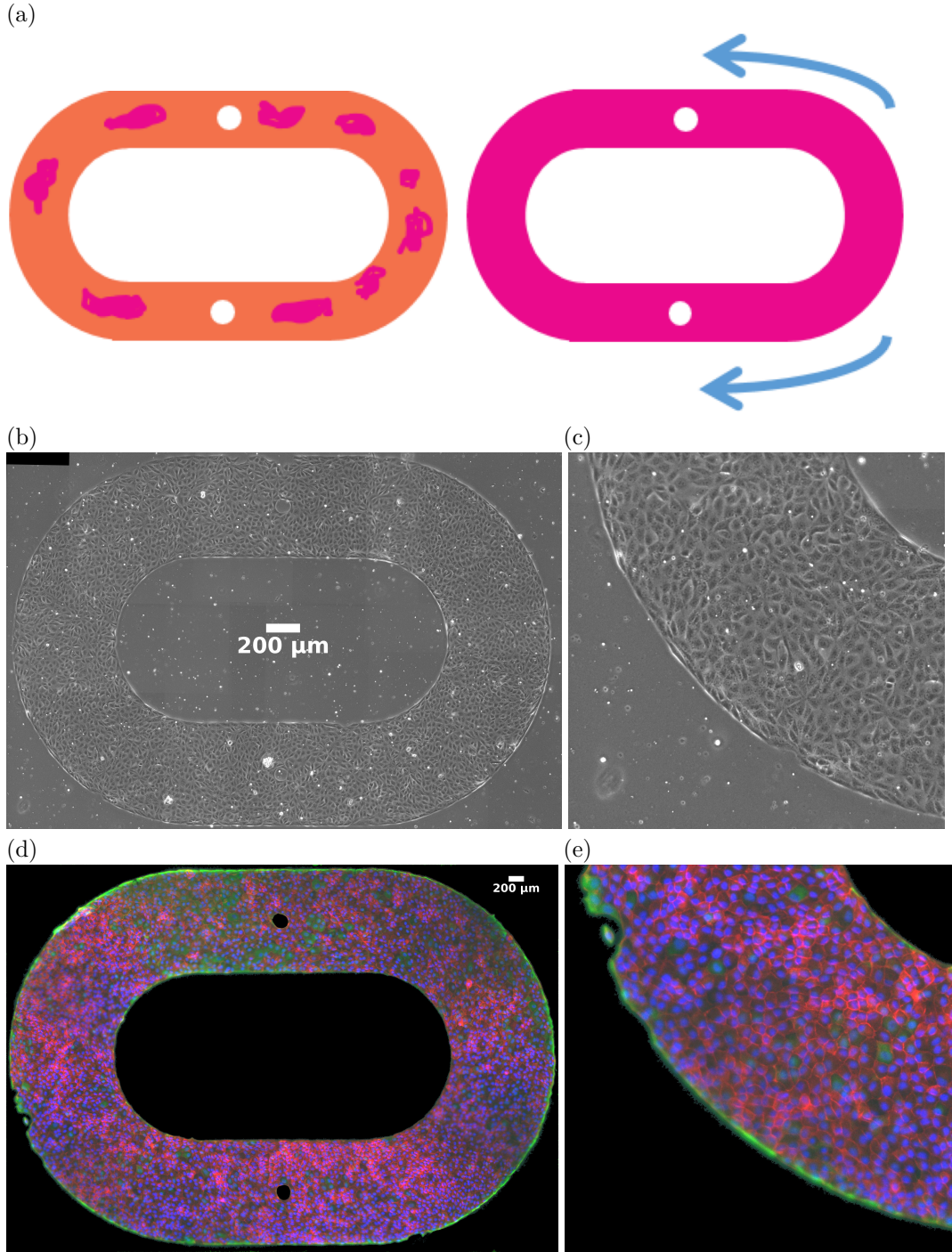


Figure 4: Racetrack setup. (a) Schematics, with adhesive substrate regions in orange when bare and in pink when covered with cells; left: at $t < 0$, i.e., before seeded cells are confluent, and at $t > 0$, cells are confluent, blue arrows represent alternate flow directions. (b) Beginning of the experiment, live imaging, phase contrast. (c) Zoom of the bottom left part of (b). (d,e) Same as (b,c), 16 h later, fixed image, triple staining: nuclei (blue), actin (red), vimentin (green). In (b-e), substrate is hard.

distance to the boundary can be fitted by a decreasing exponential (Fig. 3d,e). Strikingly, the characteristic

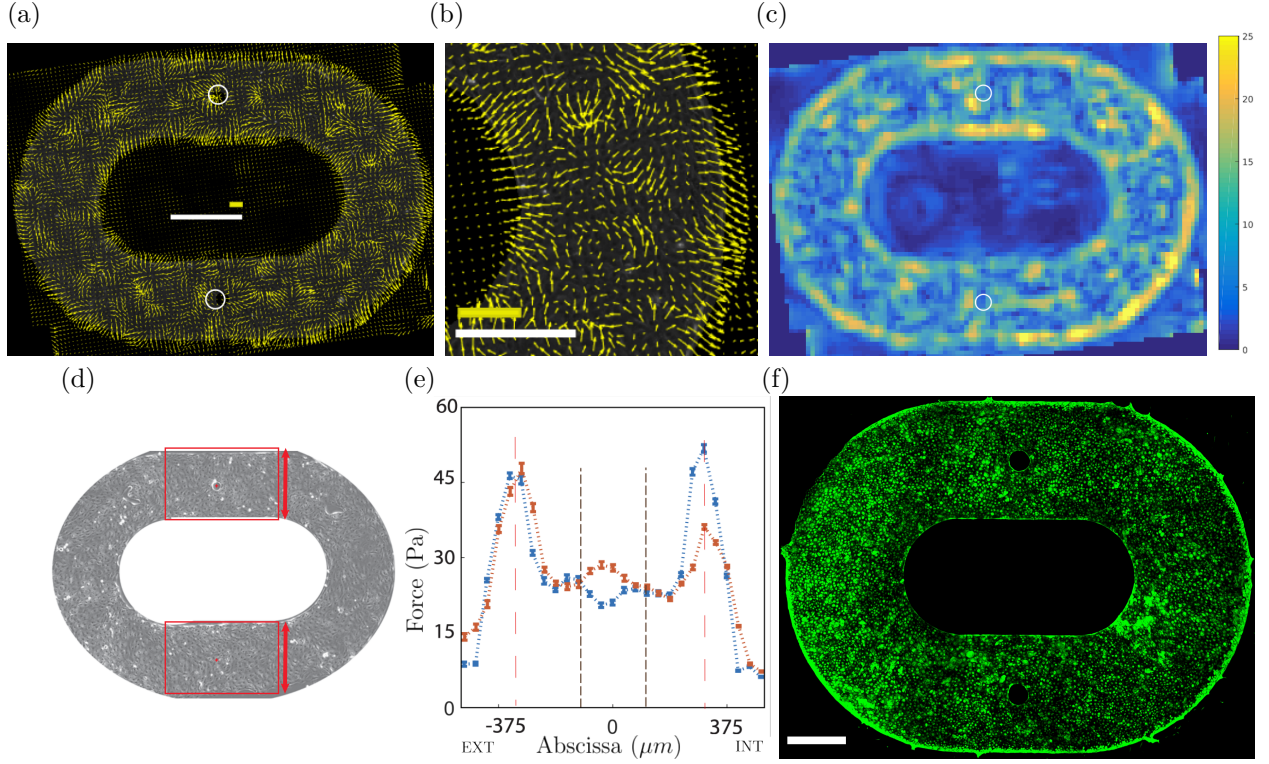


Figure 5: Traction forces on soft substrate. (a) Forces per unit area (here exerted by the substrate on the cells) in the soft racetrack, with force vectors averaged over 200-pixel boxes. White scale bar: 750 μm , yellow scale bar: 30 Pa. White circles indicate obstacle locations. (b) Zoom on the right part of (a). White scale bar: 325 μm ; yellow scale bar: 30 Pa. (c) Force magnitude, time averaged over 150 frames (~ 13 h), color coded from 0 to 60 Pa. (d) Regions of interest (rectangles of vertical width W , horizontal length $1.5 W$, centered on an obstacle), directions of measurements (arrows) and obstacles (dots). (e) Force profile across the width. Force in (a) is measured in a red rectangle in (d), averaged in space parallel to the racetrack midline, then plotted vs the distance to obstacle center along the red arrow in (d), with “EXT” outside the racetrack and “INT” inside. Bars: standard deviation of time average. Vertical dashes: obstacle (black dashes) and track (red dashes) boundaries at the beginning of the experiment. Blue curve corresponds to the top obstacle in (a), red curve to the bottom obstacle which is engulfed by the cells at long times. (f) Vimentin staining on a hard racetrack.

length near the free boundary, $65 \pm 4 \mu\text{m}$, is an order of magnitude greater than that near the confining boundary, $3.2 \pm 0.7 \mu\text{m}$.

As opposed to keratin, another intermediate filament which resists high externally applied stress or strain [42], here vimentin marks the spontaneous stress or strain internally generated by the migrating cells. Interestingly, in presence of Simvastatin, a drug that causes the vimentin network to collapse near the nucleus (without affecting microtubules or actin, and without depolymerizing vimentin) [43], cells become able to escape the patterning (data not shown).

In conclusion, in addition to defining the boundary conditions, the presence of cell front seems to affect the cell behaviour itself. The vimentin gradient possibly reveals an underlying polarizing cue on the cell velocity field. As vimentin is part of several biochemical signaling cascades, it would be interesting to obtain a spatial mapping of the RNA expression.

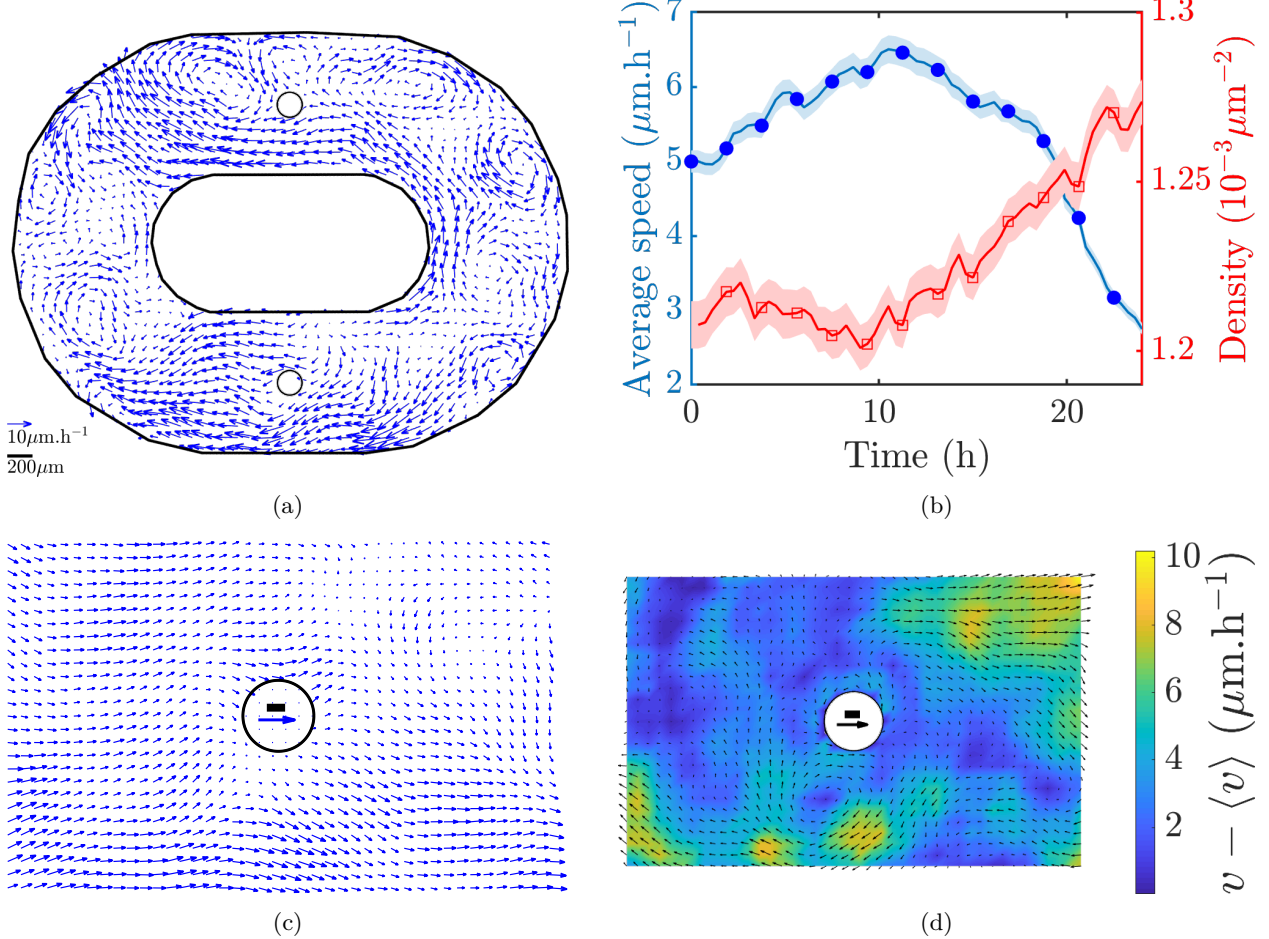


Figure 6: Velocity in a hard racetrack. (a) Velocity field averaged on 100 frames ~ 8 h (much larger than fluctuation correlation time, see Fig. 11 below). (b) Time evolution of a typical experiment. Speed (closed blue circles, left axis) and density (open red squares, right axis); averages (\pm s.e.m.) in space over ~ 1500 boxes. (c) Velocity field around an obstacle, zoom from (a). (d) Velocity field around the obstacle, same as (c) but in the virtual referential of the cell monolayer. Scale bars in (c,d): $50 \mu\text{m}$. Scale arrows in (c,d): $30 \mu\text{m.h}^{-1} = 0.5 \mu\text{m min}^{-1}$.

3 Racetrack, without front

To discriminate more clearly the cell monolayer's intrinsic bulk properties from the external impact of the free front, we removed the latter by turning to a closed geometry: the racetrack (Fig. 4). An adhesive periodic circuit is made of two half circles, linked with two straight portions in which a circular obstacle is inserted, so that we can compare the effect of different boundary curvatures: concave, flat or convex. To enable a multiscale study comparable to that of strips, we keep a large size in each of the 48 patterns. Each portion of the racetrack has a uniform width W which is chosen as: either $W \sim 600 \mu\text{m}$, in which case the midline perimeter length L is $6700 \mu\text{m}$; or $W \sim 900 - 1000 \mu\text{m}$, in which case $L = 8000 \mu\text{m}$; see substrate distributions in Table S1 and actual measurements in Fig. S1.

3.1 Forces

In the absence of significant inertia, mechano-chemical coupling relies on the equilibrium of mechanical forces. Fig. 5a-c presents the traction force distribution measured on the racetrack with a PDMS substrate soft enough (rigidity modulus: 3 kPa) that traction forces can deform it, and with $W = 600 \mu\text{m}$. As already observed by Kim *et al.* [12], significant forces are exerted on the cells by the confining boundaries,

perpendicularly to them and directed outward (i.e. cells pull inward into the tissue). Fig. 5d,e quantitatively evidences the force peak at boundaries. It is consistent with the vimentin staining peak at the same boundaries (Fig. 5f) and with the role of vimentin in force generation [39, 40].

3.2 Spontaneous velocity field

Cells are seeded at low density, and once they reach confluence spontaneous migration movements are observed (Fig. 6a). As expected [44], we do not detect any simple correlation between forces and velocities (data not shown). In two studies using annuli or racetracks up to millimeter-sized diameter, with MDCK cells [8] and with the more coordinated HBEC cells [32], the periodic boundary conditions and the non-trivial topology based on the hole in the center of the racetrack enabled a coherent cell circulation to set in.

Here cells slowly reorganize, and as time progresses, the spatially averaged velocity modulus increases during the first few hours, reaches a plateau at longer timescales, and eventually decreases (Fig. 6b), inversely correlated with spatially averaged density. A similar plateau has been observed in unconfined HBEC cells and interpreted as a jamming transition [45]. Here, the transition to slower movement is delayed thanks to mitomycin treatment. We do not detect any significant effect of confining boundary curvature, whether concave, flat or convex.

Unlike in the strip, in the racetrack the velocity field fluctuates around a zero time average and a zero space average (and we do not adimension the velocity field). Locally, due to symmetry breaking, self-organized collective cell movements appear. Within a straight portion of the racetrack, directed migration can be observed over short time and length scales, and the inserted obstacle locally probes this migration (Fig. 6c). The obstacle creates a hole, i.e. locally a non-trivial topology, and a circulation can set in (Fig. 6d).

3.3 Velocity coordination in different conditions

Migration on soft racetracks is qualitatively similar but significantly higher (Student test $p < 0.01$) than on hard substrate: there is a 50% increase in the modulus of the velocity average and 30% increase in the standard deviation of the velocity modulus, see Fig. 7.

This means that the individual cell migration velocity is higher on soft substrate, as opposed to what is usually observed with a free front (in fact, a velocity higher on soft substrate than on hard one had been reported once [41], but it was at 60 kPa, more than a decade above our rigidity modulus). It also means that the velocity fluctuates more; and also that the inter-cell coordination is higher, maybe thanks to cell-cell interactions mediated by the substrate elastic deformation [46].

Fig. 7 shows velocity and coordination are similar on strips vs racetracks. It is difficult to interpret these data because density values and initial conditions differ too much.

Fig. 7 also shows a reduction in average velocity on strip when adding three drugs (see Supp. Movies). CK666, a selective inhibitor of the Arp2/3 complex, nucleates branched actin filament networks and thus significantly impacts formation and remodeling of branched actin arrays such as those in the lamellipodia [42, 47]. The two other drugs alter the monolayer mechanical resistance [43, 48]: Nocodazole specifically binds to β -tubulin and reversibly inhibits microtubule polymerization causing rapid microtubule depolymerization; Simvastatin inhibits HMG-CoA reductase and thereby blocks the prenylation of small GTPases that regulate actin filament organization and intermediate filament dynamics.

Conversely, adding Blebbistatin, which affects myosin activity and cellular activity, increases the average velocity and its coordination. This is surprising and we speculate that the increase in coordination might be due to a decrease in cell activity fluctuations.

3.4 Velocity domains and waves

Jain *et al.* have performed experiments of MDCK migration in annuli, mainly of 200 μm in outer diameter (at most 1000 μm) and 20 μm in width (at most 200 μm) [8]. They aimed to limit cell migration along the ring to one-dimensional track, in order to minimize lateral intercellular interactions. They have observed a cell flow coordinated in the same direction over the entire tracks. In Giuglaris' PhD, similar observations have been made with more coordinated HBEC cells on racetracks up to 1800 μm in length, $W = 150 \mu\text{m}$ in width [32].

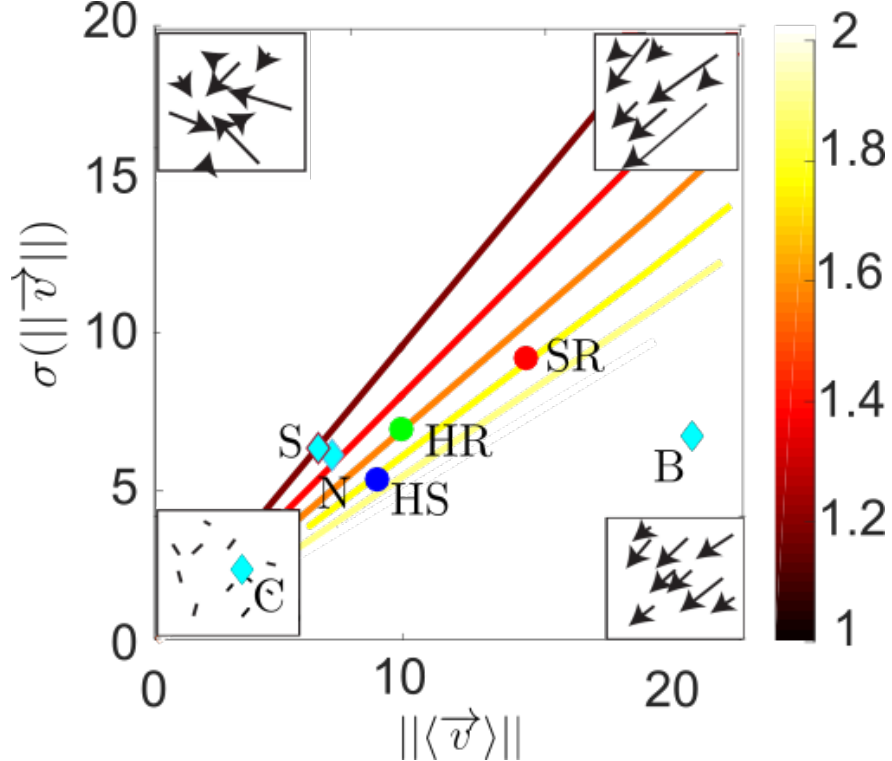


Figure 7: Velocity coordination. Phase diagram of observed velocity fields. Horizontal axis: modulus of average velocity vector ($\mu\text{m.h}^{-1}$). Vertical axis: standard deviation of the velocity modulus ($\mu\text{m.h}^{-1}$). Four extreme archetypes are schematized in the corners. To guide the eye, the coordination parameter (ratio of vertical to horizontal axis) is indicated by color-coded straight lines. Measurements without drug (circles): hard strips (HS), hard racetracks (HR), soft racetracks (SR). Measurements on racetracks are performed on a rectangle of vertical width W , horizontal length $1.5 W$, centered around a V -shaped obstacle. Measurements with drug on hard strips (lozenges): Simvasatin (S), Nocodazole (N), CK666 (C), Blebbistatin (B). Averages are performed over time (100 min, i.e. 21 frames); then each average and standard deviation is calculated over several measurements performed on the same day in the same conditions. HS, $N = 16$ ($W = 1000 \mu\text{m}$); HR, $N = 14$, with chiral V -shaped obstacle design (8 with $W = 1000 \mu\text{m}$ and 6 with $W = 600 \mu\text{m}$); SR, $N = 4$ (2 with $W = 1000 \mu\text{m}$ and 2 with $W = 600 \mu\text{m}$); drugs, $N = 4$.

Conversely, to observe the coexistence of several correlated domains, two studies have used large enough confined patterns [49, 50]. They have both evidenced velocity waves, a feature which is generic in active cell migration [31, 38, 51–53]. In one-dimensional strips up to length $L = 2000 \mu\text{m}$ and width $W = 40 \mu\text{m}$, Petrolli *et al.* observed on MDCK cells that v_x showed a multimodal standing wave with a wavelength and pulsation which both increase with L up to $L > 500 \mu\text{m}$, then plateau [49]; this led them to the hypothesis that there exists an unique tissue-intrinsic pattern length, $\sim 380 \mu\text{m}$, and time, $\sim 270 \text{ min}$. On two-dimensional rectangles up to $L = 3500 \mu\text{m}$ and $W = 1000 \mu\text{m}$, Peyret *et al.*, focusing on human keratinocytes (HaCaT) and enterocytes (Caco2), observed that v_y presented standing wave patterns with a pulsation and amplitude that were dependent on W [50]. They also observed that v_x showed a mix of propagating waves and multimodal standing waves, with a characteristic wavelength dependent on W .

We too observe domains of velocities oriented in the same direction, which alternate along the racetrack midline, schematized on Fig. 4a. This is quantified by the autocorrelation function of the velocity component parallel to the midline. The position λ of its first minimum is a robust, model-free characterisation of the typical domain length scale, especially since the minimum is pronounced. In a rare example, we observed a time evolution of λ (Fig. 8a). The velocity component perpendicular to the midline displays a similar behaviour (Fig. S2). We perform the statistics on 66 measurements stable in time (Fig. S1). When increasing

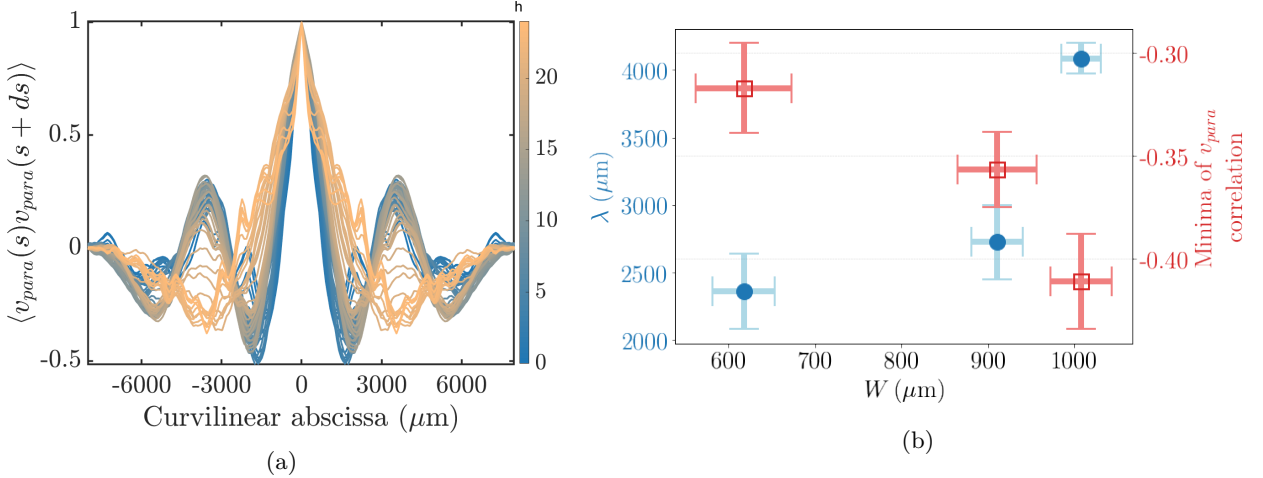


Figure 8: Spatial velocity correlations in hard racetrack. (a) Autocorrelation function of a given experiment, along the racetrack midline (curvilinear abscissa s), of the velocity component locally parallel to this midline, $v_{para}(s)$. Color code: time (h). Here $W = 1000 \mu\text{m}$, midline perimeter $L = 8000 \mu\text{m}$, symmetrized $s \rightarrow -s$. (b) Statistics of typical domain length λ (blue closed circles, left scale), and value of the first peak minimum (red open squares, right scale), vs racetrack width W . Bars are standard errors of the mean (s.e.m.).

W from $\sim 600 \mu\text{m}$ to $900\sim 1000 \mu\text{m}$, the coherence (marked by minus the minimum value of the autocorrelation) gets more and more pronounced from ~ 0.3 to ~ 0.4 (Fig. 8b). This increase in coherence is reminiscent of the increase of wave amplitude with W in Peyret *et al.*'s study [50]. We also observe that the domain size (marked by λ) increases from $\sim 1500 \mu\text{m}$ to $\sim 3000 \mu\text{m}$, suggesting that there is no unique tissue-intrinsic patterning length, and that the smallest confining length (here the width W) plays a determinant role. The characteristic time of domains is so large ($> 10-20 \text{ h}$) that we find it difficult to quantify it, except for the rare cases like in Fig. 8a. It is much larger than the period found on thinner systems by Peyret *et al.*, which is consistent with their finding that the period increases with W [50].

Symmetry breakings are limited in time and space: our experiments have large enough time-scales and length-scales to be overall symmetric in average. Obstacles do not have significant long-range effect on symmetry breaking, even if they are deliberately created with a chiral V-shaped obstacle design (see Supp. Movie 3).

3.5 Swirls, kinetic energy and enstrophy

Lin *et al.* measured the distribution of kinetic energy and enstrophy during 10 h while a monolayer was jamming [54]. They showed that both kinetic energy and enstrophy decreased with time and correlated.

Since we also observe swirls in the racetrack geometry (see Fig. 6a), we perform similar measurements over 10 h, in our case with a larger track size and without jamming. We perform 8 measurements on racetracks with different widths and circular obstacle sizes. They display the same behavior, suggesting that our results do not depend on set-up dimensions (Fig. S3a-i). We thus pool the results from all 8 measurements (Fig. 9). We observe a similar behaviour with the presence of chiral V-shaped obstacle design (Fig. S3j-l).

Figs. 9, S3 use the same representation as that of Lin *et al.* [54]. Contrary to their findings, in our case the kinetic energy and enstrophy follow a Boltzmann distribution (Fig. 9a,b). During the first 5 hours, while long-distance correlation grows, both kinetic energy and enstrophy increase; during the next 5 hours, kinetic energy still increases while enstrophy passes through a maximum and decreases (Fig. 9c).

In the future, it would be interesting to measure the Okubo-Weiss field and compare it with its measurements by Giomi [55], and to measure the radial profile of velocity in the swirls, possibly pointing to an interpretation in terms of phonon mode superposition.

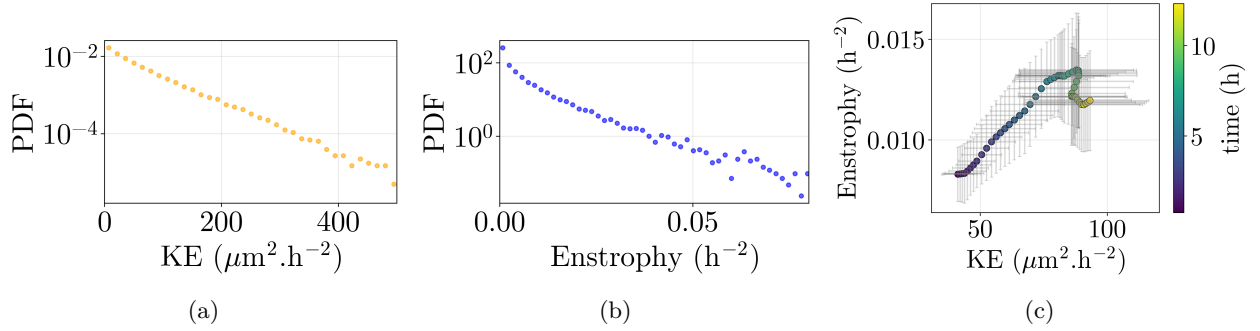


Figure 9: Kinetic energy and enstrophy. Statistics averaged in space over 64 pixels, in time over 50 frames, and over 8 measurements performed on racetracks with circular obstacles and different sizes (Fig. S3a-i). (a) PDF of kinetic energy. (b) PDF of enstrophy. (c) Enstrophy versus kinetic energy for successive times (color-coded).

4 Correlations

Taking advantage of the large length scales and long timescales of our experiments, we now investigate the velocity spatial and temporal correlation functions [56, 57].

4.1 Spatial correlations

For spatial correlations, the analysis is performed only on the hard racetrack, where it is much easier than on the strip thanks to its large size and to the absence of a steady spatial gradient, and where we realize experiments with drugs. We use the spatial correlation function defined as follows:

$$C_s(r_i, t) = \frac{\langle [\vec{V}(\vec{X}, t) - \vec{V}_0] \cdot [\vec{V}(\vec{X} + \vec{r}, t) - \vec{V}_0] \rangle_{\vec{X}}}{\langle [\vec{V}(\vec{X}, t) - \vec{V}_0]^2 \rangle_{\vec{X}}} \quad (1)$$

Here r_i is the distance between two points, $|\vec{r}|$ is in the interval $[r_i, r_{i+1}]$, $\vec{V}(\vec{X}, t)$ is the velocity field at the position \vec{X} and time t . Finally, \vec{V}_0 is the average of the velocity field, which should be chosen with care in active systems without stationarity [56]. We do not choose \vec{V}_0 to be the spatial average in a given window size dA around each point, because this would yield measurements depending on dA without any plateau (Figs. S4, S5, Section S1.4.3). We do choose \vec{V}_0 to be the time average at position \vec{X} .

Under these conditions, we find that the correlation function is a power law with a local exponent constant at small length scale (below 200 μm), which drops at larger length scales (Fig. 10). The exponent α defined as the average exponent between 30 and 200 μm varies significantly with time, indicating that the monolayer matures. It would be interesting in the future to understand this time-dependence of α , maybe due to the maturation of inter-cellular contacts. The experiment size and the addition of drugs affecting the intra-cellular mechanics have much less effect than this time-dependent maturation (Figs. S6, S7). Whatever the drug, the measurements performed after drug addition (see Supp. Movies) are not significantly different from the measurements performed just before drug addition, which themselves differ significantly from measurements performed at earlier times.

4.2 Temporal correlations

As we record cell velocity fields for several hours in strips and racetracks, we study time correlation on both (for simplicity, we have not analyzed the soft racetrack). To define the velocity field on a regular spatial grid, we average it over a spatial window of size $w_s = 32.6 \mu\text{m}$, and then over a small time window of size $w_t = 6$ frames (30 min). The temporal correlation function is then computed for different time lags τ (Fig. 11a). In a semi-logarithmic scale, the correlation function is then fitted by an exponential decay (Fig. 11b). Strikingly, we observe that for all experiments, whether strip or racetrack, the decay time is the same, ~ 100 min.

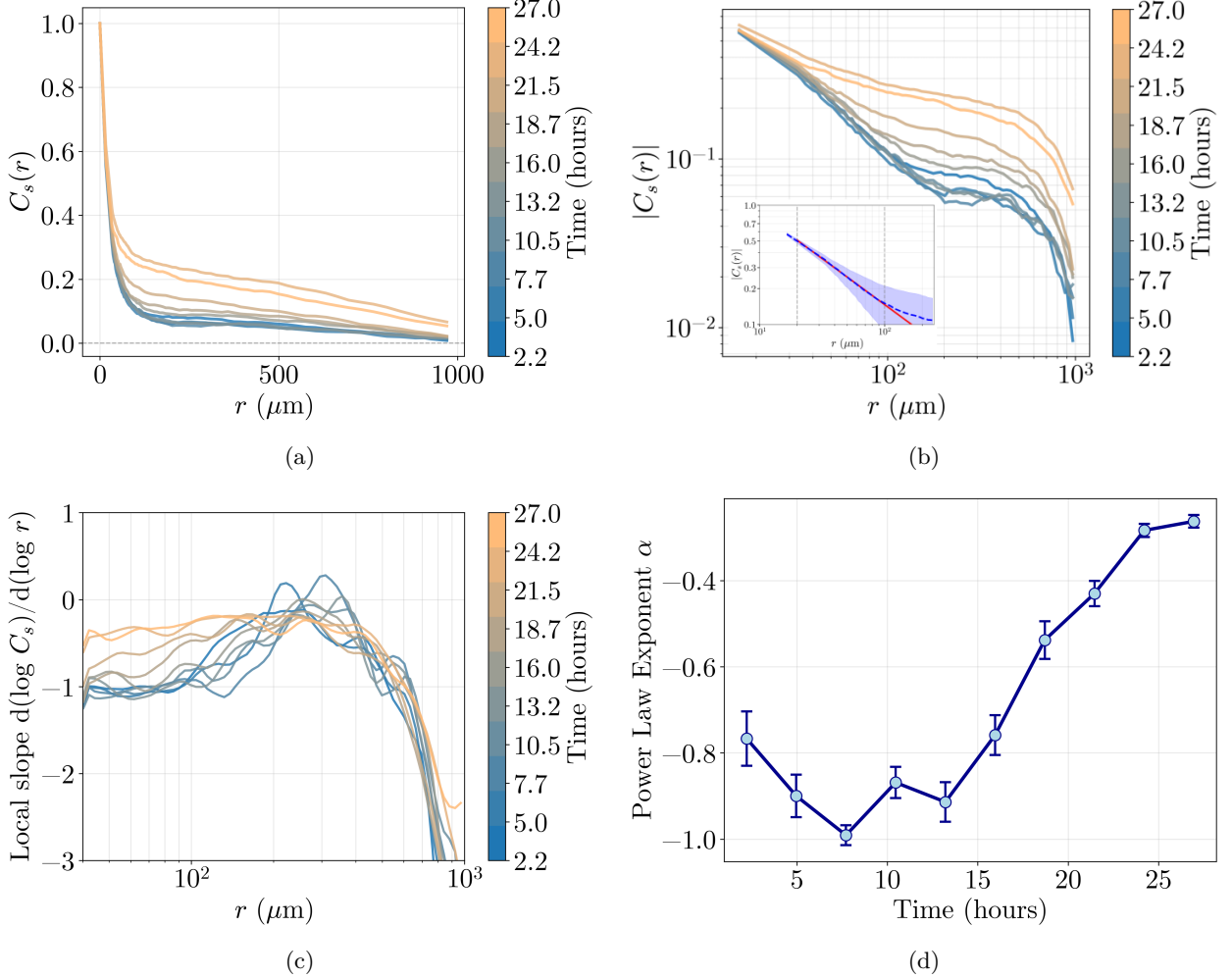


Figure 10: Temporal evolution of the velocity correlation function. Racetrack width $W = 600 \mu\text{m}$. (a) Spatial correlation function of the velocity versus distance r , for successive times color-coded from 2.2 to 27 h. (b) Same as (a) in log-log scale. Inset: spatial correlation function of the velocity averaged over all times (thick blue dashes) with its std (blue hatches); thick solid red line: linear fit to the log-log values, between $r = 20$ and $100 \mu\text{m}$ (thin vertical blue dashes). (c) Local exponent defined as the slope of (b), i.e. logarithmic derivative of (a). (d) Time evolution of exponent α , defined as the slope in (c), average (\pm s.e.m.) between $r = 30$ and $200 \mu\text{m}$.

5 Conclusion and perspectives

We perform 16 measurements using open strips with an obstacle, on hard substrates. We compare them with 66 measurements with 48 closed racetracks of different sizes, also with obstacles, on hard substrates too, and 4 using racetracks on soft substrates. This enables us to investigate and disentangle how the size, shape, topology and rigidity of patterned substrate affect the collective migration of epithelial monolayers at several space and time scales. In the future, it might be interesting to perform open strip traction force experiments on a soft substrate with different approaches, including lithography or magnetically actuated barriers.

The boundary conditions strongly affect the vimentin, which decays from the free boundary with a characteristic length $65 \pm 4 \mu\text{m}$, an order of magnitude greater than that near the confining boundary, $3.2 \pm 0.7 \mu\text{m}$. In the strip, the free front acts as a powerful external cue, imposing a global polarization and velocity gradient that dominates the tissue's intrinsic dynamics. In contrast, the periodic racetrack geometry

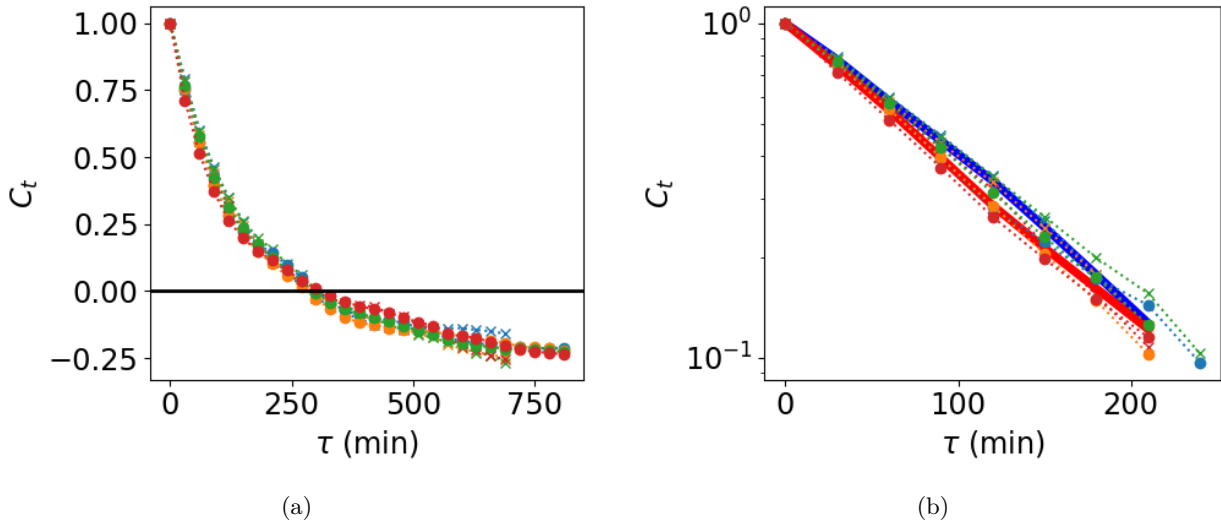


Figure 11: Temporal velocity correlation. (a) Correlation of the velocity field fluctuations around the temporal average for 4 strip measurements (crosses) and 4 hard racetrack measurements (circles). (b) Same data in semi-logarithmic scale. Solid lines: blue, average over the 4 strips; red, same for the 4 racetracks.

in absence of any net global drift isolates complex intrinsic behaviors, which are stronger on soft than on hard substrate. They are characterized by scale-free, power law fluctuating velocity domains, rather than by a single correlation length. This result suggests the monolayer behaves as a critical-like system where information is transmitted across its entire size, a feature consistent with models of active solids capable of long-range stress propagation.

Understanding the observed power-law correlations and predicting the exponent value from sub-cellular properties, as well as explaining the non-monotonous time evolution of enstrophy, are theoretical challenges. Integrating our force measurements with the velocity correlation analysis, as well as with future high-resolution imaging of molecular effectors such as vimentin or actin, might be determinant toward building a complete mechanical model connecting the tissue-scale rheology to its sub-cellular origins.

Acknowledgments

We warmly thank Sham Tlili for fruitful discussions and for her invaluable help to implement the experimental protocol. For the purpose of Open Access, a CC-BY 4.0 public copyright licence <<https://creativecommons.org/licenses/by/4.0/>> has been applied by the authors to the present document and will be applied to all subsequent versions up to the Author Accepted Manuscript arising from this submission.

Conflicts of interest

The authors have no conflicts to disclose.

Author Contribution Statement

Conceptualization: H. Delanoë-Ayari, F. Graner; Methodology: G. Duprez, M. Durande, F. Graner, H. Delanoë-Ayari; Formal analysis and investigation: G. Duprez, M. Durande, F. Graner, H. Delanoë-Ayari; Writing - original draft preparation: F. Graner, H. Delanoë-Ayari ; Resources: H. Delanoë-Ayari, F. Graner; Supervision: H. Delanoë-Ayari, F. Graner.

References

- [1] Friedl, P., Gilmour, D.: Collective cell migration in morphogenesis, regeneration and cancer. *Nature Reviews Molecular Cell Biology* **10**(7), 445–457 (2009) <https://doi.org/10.1038/nrm2720>
- [2] Rørth, P.: Collective Cell Migration. *Annual Review of Cell and Developmental Biology* **25**(Volume 25, 2009), 407–429 (2009) <https://doi.org/10.1146/annurev.cellbio.042308.113231>
- [3] Trepat, X., Wasserman, M.R., Angelini, T.E., Millet, E., Weitz, D.A., Butler, J.P., Fredberg, J.J.: Physical forces during collective cell migration. *Nature Physics* **5**(6), 426–430 (2009) <https://doi.org/10.1038/nphys1269>
- [4] Banerjee, S., Marchetti, M.C.: Continuum models of collective cell migration. In: La Porta, C.A.M., Zapperi, S. (eds.) *Cell Migrations: Causes and Functions*, pp. 45–66. Springer, Cham (2019). https://doi.org/10.1007/978-3-030-17593-1_4
- [5] La Porta, C.A.M., Zapperi, S.: Statistical features of collective cell migration. In: La Porta, C.A.M., Zapperi, S. (eds.) *Cell Migrations: Causes and Functions*, pp. 67–78. Springer, Cham (2019). https://doi.org/10.1007/978-3-030-17593-1_5
- [6] Poujade, M., Grasland-Mongrain, E., Hertzog, A., Jouanneau, J., Chavrier, P., Ladoux, B., Buguin, A., Silberzan, P.: Collective migration of an epithelial monolayer in response to a model wound. *Proceedings of the National Academy of Sciences of the United States of America*, 15988–93 (2007)
- [7] Vedula, S.R.K., Leong, M.C., Lai, T.L., Hersen, P., Kabla, A.J., Lim, C.T., Ladoux, B.: Emerging modes of collective cell migration induced by geometrical constraints. *Proceedings of the National Academy of Sciences of the United States of America* **109**(32), 12974–9 (2012) <https://doi.org/10.1073/pnas.1119313109>
- [8] Jain, S., Cachoux, V.M.L., Narayana, G.H.N.S., de Beco, S., D’Alessandro, J., Cellerin, V., Chen, T., Heuzé, M.L., Marcq, P., Mège, R.M., Kabla, A.J., Lim, C.T., Ladoux, B.: The role of single-cell mechanical behaviour and polarity in driving collective cell migration. *Nature Physics* **16**(7), 802–809 (2020) <https://doi.org/10.1038/s41567-020-0875-z>
- [9] Lo Vecchio, S., Pertz, O., Szopos, M., Navoret, L., Riveline, D.: Spontaneous rotations in epithelia as an interplay between cell polarity and boundaries. *Nature Physics* **20**(2), 322–331 (2024) <https://doi.org/10.1038/s41567-023-02295-x>
- [10] Doxzen, K., Vedula, S.R.K., Leong, M.C., Hirata, H., Gov, N.S., Kabla, A.J., Ladoux, B., Lim, C.T.: Guidance of collective cell migration by substrate geometry. *Integrative Biology* **5**(8), 1026 (2013) <https://doi.org/10.1039/c3ib40054a>
- [11] Saraswathibhatla, A., Galles, E.E., Notbohm, J.: Spatiotemporal force and motion in collective cell migration. *Scientific Data* **7**, 197–17 (2020) <https://doi.org/10.1038/s41597-020-0540-5>
- [12] Kim, J.H., Serra-Picamal, X., Tambe, D.T., Zhou, E.H., Park, C.Y., Sadati, M., Park, J.-A., Krishnan, R., Gweon, B., Millet, E., Butler, J.P., Trepat, X., Fredberg, J.J.: Propulsion and navigation within the advancing monolayer sheet. *Nature Materials* **12**(9), 856–863 (2013) <https://doi.org/10.1038/nmat3689>
- [13] Das, T., Safferling, K., Rausch, S., Grabe, N., Boehm, H., Spatz, J.P.: A molecular mechanotransduction pathway regulates collective migration of epithelial cells. *Nature Cell Biology* **17**(3), 276–287 (2015) <https://doi.org/10.1038/ncb3115> 25706233
- [14] Cochet-Escartin, O., Ranft, J., Silberzan, P., Marcq, P.: Border Forces and Friction Control Epithelial Closure Dynamics. *Biophysical Journal* **106**(1), 65–73 (2014) <https://doi.org/10.1016/j.bpj.2013.11.015>

- [15] Rausch, S., Das, T., Soiné, J.R., Hofmann, T.W., Boehm, C.H., Schwarz, U.S., Boehm, H., Spatz, J.P.: Polarizing cytoskeletal tension to induce leader cell formation during collective cell migration. *Biointerphases* **8**(1), 32 (2013) <https://doi.org/10.1186/1559-4106-8-32>
- [16] Chepizhko, O., Lionetti, M.C., Malinverno, C., Giampietro, C., Scita, G., Zapperi, S., La Porta, C.A.M.: From jamming to collective cell migration through a boundary induced transition. *Soft Matter* **14**(19), 3774–3782 (2018) <https://doi.org/10.1039/C8SM00128F>
- [17] Alert, R., Blanch-Mercader, C., Casademunt, J.: Active Fingering Instability in Tissue Spreading. *Physical Review Letters* **122**(8), 088104 (2019) <https://doi.org/10.1103/PhysRevLett.122.088104>
- [18] Reffay, M., Petitjean, L., Coscoy, S., Grasland-Mongrain, E., Amblard, F., Buguin, A., Silberzan, P.: Orientation and polarity in collectively migrating cell structures: Statics and dynamics. *Biophysical Journal* **100**(11), 2566–2575 (2011) <https://doi.org/10.1016/j.bpj.2011.04.047>
- [19] Deng, Y., Levine, H., Mao, X., Sander, L.M.: Collective motility and mechanical waves in cell clusters. *European Physical Journal E* **44**(11), 1–15 (2021) <https://doi.org/10.1140/epje/s10189-021-00141-7>
- [20] Pérez-González, C., Alert, R., Blanch-Mercader, C., Gómez-González, M., Kolodziej, T., Bazellieres, E., Casademunt, J., Trepat, X.: Active wetting of epithelial tissues. *Nature Physics* **15**(1), 79–88 (2019) <https://doi.org/10.1038/s41567-018-0279-5>
- [21] Mishra, A.K., Campanale, J.P., Mondo, J.A., Montell, D.J.: Cell interactions in collective cell migration. *Development* **146**(23), 172056 (2019) <https://doi.org/10.1242/dev.172056>
- [22] Christiansen, J.J., Rajasekaran, A.K.: Reassessing Epithelial to Mesenchymal Transition as a Prerequisite for Carcinoma Invasion and Metastasis. *Cancer Research* **66**(17), 8319–8326 (2006) <https://doi.org/10.1158/0008-5472.CAN-06-0410>
- [23] Friedl, P., Locker, J., Sahai, E., Segall, J.E.: Classifying collective cancer cell invasion. *Nature Cell Biology* **14**(8), 777–783 (2012) <https://doi.org/10.1038/ncb2548>
- [24] Tlili, S., Gauquelin, E., Li, B., Cardoso, O., Ladoux, B., Delanoë-Ayari, H., Graner, F.: Collective cell migration without proliferation: Density determines cell velocity and wave velocity. *Royal Society Open Science* **5**(5), 172421 (2018) <https://doi.org/10.1098/rsos.172421>
- [25] Hiraiwa, T.: Dynamic self-organization of migrating cells under constraints by spatial confinement and epithelial integrity. *European Physical Journal E* **45**(2), 1–16 (2022) <https://doi.org/10.1140/epje/s10189-022-00161-x>
- [26] Khalilgharibi, N., Fouchard, J., Recho, P., Charras, G., Kabla, A.: The dynamic mechanical properties of cellularised aggregates. *Current Opinion in Cell Biology* **42**, 113–120 (2016) <https://doi.org/10.1016/j.ceb.2016.06.003>
- [27] Angelini, T.E., Hannezo, E., Trepat, X., Marquez, M., Fredberg, J.J., Weitz, D.A.: Glass-like dynamics of collective cell migration. *Proceedings of the National Academy of Sciences* **108**(12), 4714–4719 (2011) <https://doi.org/10.1073/pnas.1010059108>
- [28] Armengol-Collado, J.-M., Carenza, L.N., Giomi, L.: Hydrodynamics and multiscale order in confluent epithelia. *eLife* **13**, 86400 (2024) <https://doi.org/10.7554/eLife.86400>
- [29] Balasubramaniam, L., Doostmohammadi, A., Saw, T.B., Narayana, G.H.N.S., Mueller, R., Dang, T., Thomas, M., Gupta, S., Sonam, S., Yap, A.S., Toyama, Y., Mège, R.-M., Yeomans, J.M., Ladoux, B.: Investigating the nature of active forces in tissues reveals how contractile cells can form extensile monolayers. *Nature Materials* **20**(8), 1156–1166 (2021) <https://doi.org/10.1038/s41563-021-00919-2>

- [30] Tlili, S., Gay, C., Graner, F., Marcq, P., Molino, F., Saramito, P.: Colloquium: Mechanical formalisms for tissue dynamics. *European Physical Journal E* **38**(5), 1–31 (2015) <https://doi.org/10.1140/epje/i2015-15033-4>
- [31] Tlili, S., Durande, M., Gay, C., Ladoux, B., Graner, F., Delanoë-Ayari, H.: Migrating Epithelial Monolayer Flows Like a Maxwell Viscoelastic Liquid. *Physical Review Letters* **125**(8), 088102 (2020) <https://doi.org/10.1103/PhysRevLett.125.088102>
- [32] Giuglaris, C.: Controlling collective cell migration with multiscale cues (Contrôle de la migration cellulaire collective dans des environnements multi-échelles), Paris Sciences et Lettres, Physique en Ile-de-France, under temporary embargo. PhD thesis (2024)
- [33] Lucas, B.D., Kanade, T.: An iterative image registration technique with an application to stereo vision. In: Proceedings of the 7th Joint Conference on Artificial Intelligence, Vancouver, 24–28 August 1981, pp. 674–679. Morgan Kaufmann Publishers, San Francisco (1981)
- [34] Bouguet, J.-Y.: Pyramidal Implementation of the Lucas Kanade Feature Tracker Description of the Algorithm. Intel Corporation Microprocessor Research Labs, http://robots.stanford.edu/cs223b04/algo_tracking.pdf (1999)
- [35] Beatrici, C., Kirch, C., Henkes, S., Graner, F., Brunnet, L.: Comparing individual-based models of collective cell motion in a benchmark flow geometry. *Soft Matter* **19**(29), 5583–5601 (2023) <https://doi.org/10.1039/D3SM00187C>
- [36] Cheddadi, I., Saramito, P., Dollet, B., Raufaste, C., Graner, F.: Understanding and predicting viscous, elastic, plastic flows. *European Physical Journal E* **34**, 1–15 (2011)
- [37] Hino, N., Rossetti, L., Marín-Llauradó, A., Aoki, K., Trepaut, X., Matsuda, M., Hirashima, T.: ERK-Mediated Mechanochemical Waves Direct Collective Cell Polarization. *Developmental Cell* **53**(6), 646–6608 (2020) <https://doi.org/10.1016/j.devcel.2020.05.011>
- [38] Boocock, D., Hino, N., Ruzickova, N., Hirashima, T., Hannezo, E.: Theory of mechano-chemical patterning and optimal migration in cell monolayers. *Nature Physics* **17**, 267–274 (2021) <https://doi.org/10.1038/s41567-020-01037-7>
- [39] Wu, H., Shen, Y., Sivagurunathan, S., Weber, M.S., Adam, S.A., Shin, J.H., Fredberg, J.J., Medalia, O., Goldman, R., Weitz, D.A.: Vimentin intermediate filaments and filamentous actin form unexpected interpenetrating networks that redefine the cell cortex. *Proceedings of the National Academy of Sciences* **119**(10), 2115217119 (2022) <https://doi.org/10.1073/pnas.2115217119>
- [40] Nunes Vicente, F., Lelek, M., Tinevez, J.-Y., Tran, Q.D., Pehau-Arnaudet, G., Zimmer, C., Etienne-Manneville, S., Giannone, G., Leduc, C.: Molecular organization and mechanics of single vimentin filaments revealed by super-resolution imaging. *Science Advances* **8**(8), 2696 (2022) <https://doi.org/10.1126/sciadv.abm2696>
- [41] Balcioglu, H.E., Balasubramaniam, L., Stirbat, T.V., Doss, B.L., Fardin, M.-A., Mège, R.-M., Ladoux, B.: A subtle relationship between substrate stiffness and collective migration of cell clusters. *Soft Matter* **16**(7), 1825–1839 (2020)
- [42] Latorre, E., Kale, S., Casares, L., Gómez-González, M., Uroz, M., Valon, L., Nair, R.V., Garreta, E., Montserrat, N., del Campo, A., Ladoux, B., Arroyo, M., Trepaut, X.: Active superelasticity in three-dimensional epithelia of controlled shape. *Nature* **563**(7730), 203–208 (2018) <https://doi.org/10.1038/s41586-018-0671-4>
- [43] Trogden, K.P., Battaglia, R.A., Kabiraj, P., Madden, V.J., Herrmann, H., Snider, N.T.: An image-based small-molecule screen identifies vimentin as a pharmacologically relevant target of simvastatin in

- cancer cells. *The FASEB Journal* **32**(5), 2841 (2018)
- [44] Green, Y., Fredberg, J.J., Butler, J.P.: Relationship between velocities, tractions, and intercellular stresses in the migrating epithelial monolayer. *Physical Review E* **101**(6), 062405 (2020) <https://doi.org/10.1103/PhysRevE.101.062405>
- [45] Garcia, S., Hannezo, E., Elgeti, J., Joanny, J.-F., Silberzan, P., Gov, N.S.: Physics of active jamming during collective cellular motion in a monolayer. *Proceedings of the National Academy of Sciences* **112**(50), 15314–15319 (2015) <https://doi.org/10.1073/pnas.1510973112>
- [46] Bischofs, B., Safran, S.A., Schwarz, U.S.: Elastic interactions of active cells with soft materials. *Physical Review E* **69**(2), 021911 (2004)
- [47] Chen, T., Callan-Jones, A., Fedorov, E., Ravasio, A., Brugués, A., Ong, H.T., Toyama, Y., Low, B.C., Trepat, X., Shemesh, T.: Large-scale curvature sensing by directional actin flow drives cellular migration mode switching. *Nature Physics* **15**(4), 393–402 (2019)
- [48] Chang, Y.-C., Nalbant, P., Birkenfeld, J., Chang, Z.-F., Bokoch, G.M.: GEF-H1 couples nocodazole-induced microtubule disassembly to cell contractility via RhoA. *Molecular Biology of the Cell* **19**, 2147–2153 (2008)
- [49] Petrolli, V., Le Goff, M., Tadrous, M., Martens, K., Allier, C., Mandula, O., Hervé, L., Henkes, S., Sknepnek, R., Boudou, T., Cappello, G., Balland, M.: Confinement-Induced Transition between Wavelike Collective Cell Migration Modes. *Physical Review Letters* **122**(16), 168101 (2019) <https://doi.org/10.1103/PhysRevLett.122.168101>
- [50] Peyret, G., Mueller, R., d'Alessandro, J., Begnaud, S., Marcq, P., Mège, R.-M., Yeomans, J.M., Doostmohammadi, A., Ladoux, B.: Sustained Oscillations of Epithelial Cell Sheets. *Biophysical Journal* **117**(3), 464–478 (2019) <https://doi.org/10.1016/j.bpj.2019.06.013>
- [51] Yabunaka, S., Marcq, P.: Emergence of epithelial cell density waves. *Soft Matter* **13**, 7046–7052 (2017) <https://doi.org/10.1039/C7SM01172E>
- [52] Blanch-Mercader, C., Casademunt, J.: Hydrodynamic instabilities, waves and turbulence in spreading epithelia. *Soft Matter* **13**(38), 6913–6928 (2017) <https://doi.org/10.1039/C7SM01128H>
- [53] Boocock, D., Hirashima, T., Hannezo, E.: Interplay between Mechanochemical Patterning and Glassy Dynamics in Cellular Monolayers. *PRX Life* **1**(1), 013001 (2023) <https://doi.org/10.1103/PRXLife.1.013001>
- [54] Lin, S.-Z., Zhang, W.-Y., Bi, D., Li, B., Feng, X.-Q.: Energetics of mesoscale cell turbulence in two-dimensional monolayers. *Communications Physics* **4**, 21 (2021) <https://doi.org/10.1038/s42005-021-00530-6>
- [55] Giomi, L.: Geometry and topology of turbulence in active nematics. *Physical Review X* **5**, 031003 (2015) <https://doi.org/10.1103/PhysRevX.5.031003>
- [56] Cavagna, A., Giardina, I., Grigera, T.S.: The physics of flocking: Correlation as a compass from experiments to theory. *Physics Reports* **728**, 1–62 (2018) <https://doi.org/10.1016/j.physrep.2017.11.003>
- [57] Vicsek, T., Zafeiris, A.: Collective motion. *Physics Reports* **517**(3), 71–140 (2012) <https://doi.org/10.1016/j.physrep.2012.03.004>
- [58] Várkuti, B.H., Képíró, M., Horváth, I.Á., Végner, L., Ráti, S., Zsigmond, Á., Hegyi, G., Lenkei, Z., Varga, M., Málnási-Csizmadia, A.: A highly soluble, non-phototoxic, non-fluorescent blebbistatin

- derivative. *Scientific Reports* **6**(1), 26141 (2016)
- [59] Butler, J.P., Tolić-Nørrelykke, I.M., Fabry, B., Fredberg, J.J.: Traction fields, moments, and strain energy that cells exert on their surroundings. *American Journal of Physiology-Cell Physiology* **282**(3), 595–605 (2002) <https://doi.org/10.1152/ajpcell.00270.2001>
- [60] Hansen, P.C.: *Discrete Inverse Problems: Insight and Algorithms*. Society for Industrial and Applied Mathematics, Philadelphia (2010). <https://doi.org/10.1137/1.9780898718836>
- [61] Huber, P.J., Ronchetti, E.M.: *Robust Statistics*. John Wiley & Sons, Hoboken (2011)
- [62] HuberRegressor. https://scikit-learn.org/stable/modules/generated/sklearn.linear_model.HuberRegressor.html

Supplementary Materials

“Geometric Confinement Reveals Scale-Free Velocity Correlations in Epithelial Cell Monolayer”

Guillaume Duprez, Mélina Durande, François Graner, Hélène Delanoë-Ayari

S1 Materials and Methods

S1.1 Cell monolayer experiments

S1.1.1 Cell culture

We use the same MDCK cell line as in Ref. [7]. Cells are seeded on the patterned substrates one to two days before starting the experiment, until they reach confluence. We then add mitomycin C (Sigma M4287) at a concentration of 8 µg/ml.

S1.1.2 Patterning on hard PDMS substrate

We use the same protocol as described in detail in Ref. [24]. Patterned PDMS stamps prepared from silanized wafers are incubated for 45 min at 37°C or 60 min at room temperature with a 60 µL drop of 50 µg/mL fibronectin solution (Gibco Ref. 33010-018).

A thin layer of rigid PDMS (10% of cross-linking agent) is spin-coated on a glass coverslip (#1, diameter 30 mm). We use a velocity of 500 rpm for 10 s followed by 30 s at 1000 rpm. We aim to reach a thickness of around 200 µm. The glass coverslip is then glued (using Loctite Si 5398) to a custom-drilled Petri dish and cured overnight at 65°C. Just before patterning, we then expose the sample to UV-ozone for approximately 20 min to activate the PDMS surface. After incubation, stamps are immersed extremely briefly in deionized water, then dried with pressurized air and pressed on the UV-activated PDMS surface to transfer fibronectin. A 2% Pluronic F-127 (Sigma) solution is added to the Petri dish to chemically block the regions outside of the fibronectin pattern for 1 h at room temperature. The Pluronic solution is removed after 1 h and the Petri dish is rinsed three to six times with a PBS solution.

The dimensions of the racetrack widths and obstacle diameters are listed on Table S1.

W	D	V	N
1000	300	yes	5
1000	160	yes	4
1000	300	no	7
1000	160	no	7
600	80	yes	7
600	80	no	5
600	80	no	13

Table S1: List of 48 hard racetrack substrates. W : Racetrack width (µm). D : obstacle diameter (µm). V: presence of chiral V-shaped obstacle design. N : number of racetracks.

S1.2 Live Microscopy

For long-term imaging, we employ phase contrast microscopy at 10X magnification. Pixel size is 0.645 µm. Under the most optimistic assumptions, it is possible to acquire data from six samples in parallel, with each sample containing either four bands or four racetracks. This setup allows for up to 24 experiments to be

conducted simultaneously during a single acquisition session. However, two main experimental limitations arise in practice. The first is that obtaining six perfectly synchronized and high-quality experiments is rare. The second limitation stems from the imaging time required to cover all samples within a time frame of less than 5 min. This constraint is critical to accurately capture the dynamics of cellular movement and to enable temporal averaging of the results.

To image a single band, three microscope fields of 2048×2048 pixels must be captured. In contrast, imaging a single racetrack requires between 10 and 20 fields. The positions of each field are manually marked, ensuring sufficient overlap between adjacent images. Subsequently, a custom Micro-Manager script, designed to enhance software stability, automatically moves through the fields at regular intervals. As a result, a sample contains between 12 fields (if composed exclusively of bands) and up to 80 fields (if containing racetracks).

The list of actual measurements on racetracks (Fig. S1) differs from that of racetrack substrates (Table S1) for two reasons. First, there is some spreading in dimensions. Second, for each substrate we perform one or more measurements, selected as time sequences during which the velocity field is stable in time.

S1.2.1 Soft PDMS substrate

For traction force microscopy we used Dow Corning Toray CY 52-276 A/ Dow Corning Toray CY 52-276 B, mixed at a ratio 5:5, which exhibits a Young modulus of approximately 3 kPa (measured using a commercial rheometer). Between 0.1 and 0.2 g of this PDMS is deposited onto a commercial glass-bottom Petri dishes (Nunc 27 mm) and allowed to spread naturally by viscosity over approximately one hour before curing at 65°C for 17 min. This process results in a working thickness of the PDMS layer of about $100\ \mu\text{m}$. The surface is then silanized in liquid phase using Sigma reagent 440140 at 5% in absolute ethanol to activate it for covalent bonding with the beads. After rinsing three times with 95% ethanol to ensure homogeneous wetting without droplets, the substrate is dried in an oven at 60°C for 30 min. The bead solution, diluted 1/250, is incubated on the surface at room temperature for 5 min, followed by three rinses with distilled water. To reduce the stickiness of the beads, they are passivated with a Tris solution for 20 min at room temperature, and finally dried at 60°C for 15 min.

This PDMS is very soft, fragile and sticky. Despite numerous attempts, we have not been able yet to find a method to place and remove a stamp without damaging either the cell monolayer or the PDMS substrate. This has prevented us from performing reproducible, unbiased open strip traction force experiments.

S1.2.2 Immunofluorescence

After approximately 24 hours of acquisition, the samples are fixed and stained to visualize different cellular components, as follows. First, the samples are quickly rinsed with PBS. Next, they are fixed with 4% PFA for 20 min. This is followed by three PBS rinses for 5 min each, during which the cells are permeabilized with 0.1% Triton X-100. Finally, the samples are rinsed three more times with PBS for 5 min each. Vimentin is stained with a primary antibody raised in rabbit (1/250 concentration) overnight, followed by a secondary goat anti-rabbit antibody (1/500 concentration) for 1 hour. The staining is performed at 4°C when done overnight, and at room temperature otherwise. Finally, the samples are stored in a cool environment for several months, ensuring they do not dry out.

S1.2.3 Other drugs

Drugs other than mitomycin are added to the cell culture medium once migration has already significantly begun. Incubation is performed at 37°C for 1 hour, followed by multiple rinses.

To disrupt the microtubule network, Nocodazole (Sigma: M1404) at $0.5\ \mu\text{g}/\text{mL}$ is used [48]. To affect the branched actin network, CK666 (Sigma: SML0006) at $100\ \mu\text{M}$ is used [42, 47]. To disrupt the vimentin network, Simvastatin (Tocris: 1965/50) at $10\ \mu\text{M}$ is used [43]. Finally, to affect myosin activity and cellular activity, para-amino-Blebbistatin (Axol ax494682) at $50\ \mu\text{M}$ is used. It has the advantage of being much more stable and less phototoxic than traditional Blebbistatin [58].

S1.3 Preparation of Products

S1.3.1 Preparation of a Polyvinyl Alcohol (PVA) membrane

A solution is prepared by mixing 0.5 g of PVA in 20 mL of pure water, while stirring and heating (approximately 80°C) until fully dissolved (typically within 5 to 6 hours). The solution is then filtered using a 0.22 μm filter and poured into a 10 cm diameter Petri dish. The membrane is dried under a fume hood with the lid slightly ajar to allow airflow while minimizing exposure. This method helps to prevent the formation of ripples on the surface of the membrane. The membrane is stored for one to two weeks, wrapped in parafilm to prevent excessive drying.

S1.3.2 Preparation of the bead solution

To prepare the bead solution, 3.8 mg/mL of sodium tetraborate and 5 mg/mL of boric acid are dissolved in distilled water with all necessary precautions. This mixture is stirred until fully dissolved overnight under a fume hood. The undiluted bead solution is then sonicated for 10 min before being added to the medium at the desired concentration (1/250 or 1/500). This mixture remains stable for at least one month.

Immediately before an experiment, the bead solution is sonicated for 5 min to ensure proper homogenization and to detach any aggregated beads. Just before contact with the substrate, EDC (Sigma E7750) is added at a concentration of 0.1 mg/mL. EDC degrades extremely quickly in a basic environment but acts as a potent catalyst when added to the medium immediately before use.

S1.3.3 Preparation of Pluronic solution

A 2% Pluronic solution is prepared by mixing 1 g of Pluronic in 50 mL of distilled water and stirring until fully dissolved. The solution is then filtered using a 0.22 μm filter.

S1.3.4 Indirect printing of protein patterns

For indirect printing on a soft substrate, the process begins by preparing the PVA membrane (see Section S1.3.1). A PDMS stamp is prepared in the same way as for rigid PDMS surface stamping. Subsequently, the stamp is placed on the PVA membrane for approximately 5 min, allowing the adhesion proteins to adsorb onto the PVA surface. The membrane is then carefully cut around the stamps, and the stamps are peeled off the membrane.

The next step involves placing the membrane face down onto the PDMS with great care to ensure that the proteins adsorb onto the PDMS rather than on the PVA. The PVA is dissolved while passivating the surface with a 2% Pluronic solution for 2 hours. Finally, the surface is rinsed 6 to 7 times with PBS, taking care never to let the surface dry.

S1.3.5 Surface passivation

At this stage, a glass surface with PDMS with the printed pattern is obtained. The final step before cell deposition involves passivating this surface to prevent cells from adhering to areas without adhesion proteins. For this purpose, Pluronic is used; this hydrophilic surfactant binds to the fibronectin-free areas and blocks cell access to these regions. The surface is incubated with a 2% Pluronic solution in PBS for 2 hours before rinsing it 6 or 7 times with PBS to remove residual cytotoxicity.

S1.4 Data Analysis

S1.4.1 Velocity measurements

The Kanade-Lucas-Tomasi (KLT) algorithm [33, 34] tracks object velocities by searching for pixels with high local intensity gradients. A fixed-size window of 64 pixels is defined, and the algorithm seeks the correspondence of points within this window in the subsequent image. The algorithm is pyramidal: recognition is performed on images of different successive resolutions with identical window sizes. Starting from the lowest resolution, large-scale movements are traced, and as the resolution increases, the displacement measurement is refined. This method allows for cell tracking, providing a Lagrangian approach to displacement. Eulerian

analysis is possible by interpolating or averaging the results on a fixed grid. In practice, the steps are as follows.

First, all microscopy fields at a given time are stitched together to create a large image. Points in these large images, for which the KLT is calculated, are defined by searching for local maxima in the last image. The KLT is used as a backward particle tracking method (from the end to the beginning). We select 50,000 points, which mainly correspond to cell edges, and exclude those that are too close to each other (less than 15 pixels apart).

Once all points are defined in the last image, the KLT calculation is performed by returning to the initial fields. Because of frame stitching, some overlap can occur; for points present in the overlap region, their velocities on both frames are averaged.

Finally, the points are moved according to the found velocity vector, and the KLT calculation steps are repeated. The local maxima are calculated only once, during the first pass of the algorithm.

S1.4.2 Traction Force Microscopy

The relationship between the traction field $\mathbf{t}(\mathbf{x})$ exerted by the cells and the substrate displacement field $\mathbf{u}(\mathbf{x})$ measured experimentally can be expressed as a convolution with the elastic Green tensor G_{ij} , where i, j are cartesian coordinates:

$$u_i(\mathbf{x}) = \int G_{ij}(\mathbf{x} - \mathbf{x}') t_j(\mathbf{x}') d\mathbf{x}', \quad (2)$$

The coefficients of \mathbf{G} are derived from the Boussinesq solution for an isotropic, linearly elastic half-space characterized by the Young modulus E and the Poisson ratio ν . We used Fast Fourier Transform, following Butler [59] to compute cell-matrix stresses from the displacement field.

Direct inversion of \mathbf{G} provides an unregularized solution that is highly sensitive to experimental noise, rendering the problem ill-posed and non-unique. To overcome this limitation, a truncated singular value decomposition (tSVD) regularization is applied [60]. The singular values of \mathbf{G} are ordered in decreasing magnitude, and the truncation point is identified from the maximum of the second derivative of their distribution, effectively filtering out the small eigenvalues associated with high-frequency components. This approach smooths the reconstructed traction field while preserving its essential spatial structure, ensuring a stable and robust inversion.

S1.4.3 Spatial correlation function

Two parameters strongly affect the correlation function of the velocity field fluctuations: (i) the size dA of spatial averaging window, and (ii) the size of the box on which the correlation is calculated. Importantly, to avoid artifacts, in each box we normalize the fluctuations by the average velocity squared measured in this box.

The spatial correlation function is a function of the distance between two points. In the racetrack case, if we use Cartesian coordinates the correlation will be performed without regard for the physical meaning: two points could be considered as correlated even if the direct path between them is the central zone void of cells.

First, we use the classical method of calculation, by calculating the correlation function on squared interrogation windows (Fig. S4a). We first choose what we expect to be a sufficiently large one, i.e., $1300 \mu\text{m}$ (Fig. S4b). To increase the statistics, we repeat the same measurement all along the racetrack, and reach a plateau (Fig. S4c).

Second, to take advantage of the largest possible interrogation window, we unwrap and flatten the racetrack. To do so, we define a local system of coordinates respectuous of the racetrack topology, using the curvilinear abscissa s (i.e. the projected position onto the racetrack midline) and the distance to this line. We then obtain a rectangle with periodic boundary conditions (see Fig. S5a, and estimations of the error it entails). Performing again the correlation function calculation (Fig. S5b), this time we no longer reach any plateau (Fig. S5c).

Fitting a power law to the correlation function is performed using a robust regression technique: the Huber regressor [61], which is part of the `scikit-learn` library [62]. It minimizes the least square residues, and modifies the loss function to down-weight outliers, providing a more reliable fit in the presence of noisy data.

S2 Supplementary Figures

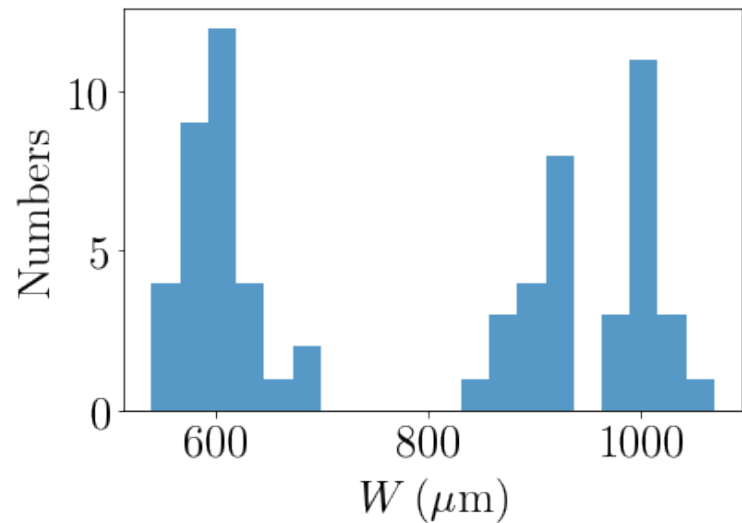


Figure S1: Racetrack measurements. Distribution of 66 actual measurements on hard racetrack substrates (see Table S1).

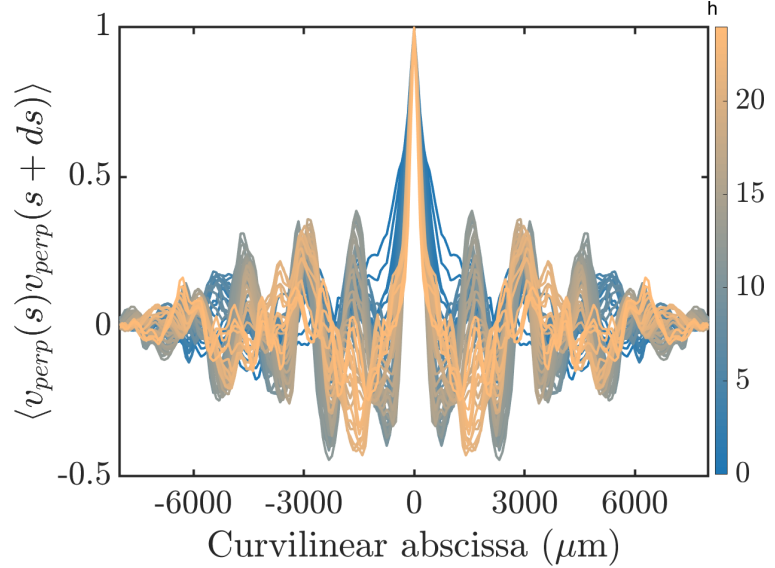


Figure S2: Perpendicular velocity autocorrelation. Autocorrelation function along the racetrack midline (curvilinear abscissa s), of the velocity component locally perpendicular to this midline, $v_{perp}(s)$. Color code: time (h). Same racetrack as in Fig. 8a, $W = 1000 \mu\text{m}$, midline perimeter $8200 \mu\text{m}$, symmetrized $s \rightarrow -s$.

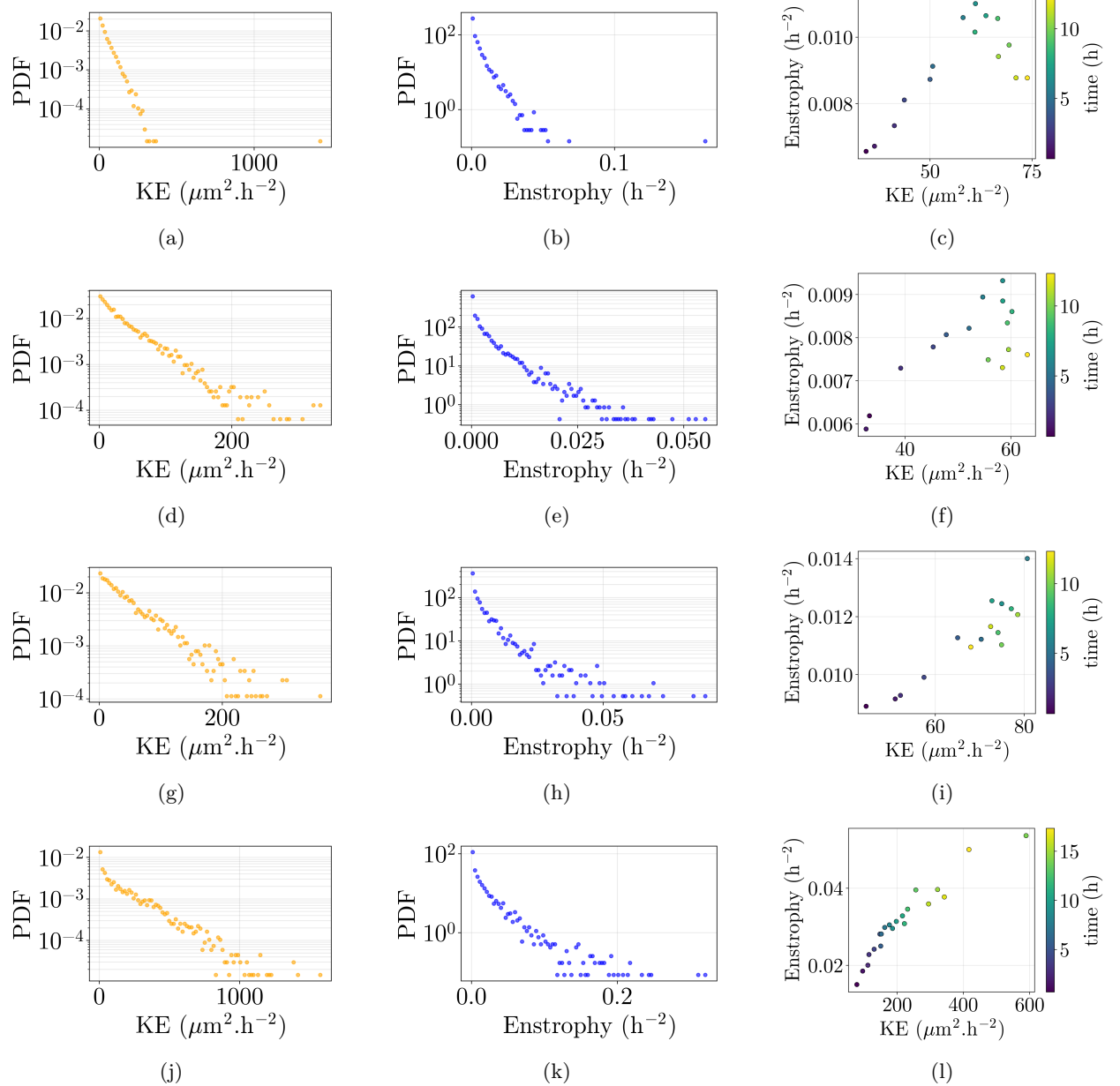


Figure S3: Kinetic energy and enstrophy for different racetracks geometries, not averaged over measurements. Statistics averaged in space over 64 pixels, in time over 50 frames. Same representation as Fig. 9. **(a-c)** Racetrack, width $W = 1000 \mu\text{m}$, obstacle diameter $D = 160 \mu\text{m}$. **(a)** PDF of kinetic energy; **(b)** PDF of enstrophy; **(c)** Enstrophy versus kinetic energy for successive times (color-coded). **(d-f)** Same for $W = 1000 \mu\text{m}$, $D = 300 \mu\text{m}$. **(g-i)** Same for $W = 600 \mu\text{m}$, $D = 160 \mu\text{m}$. **(j-l)** Same for $W = 1000 \mu\text{m}$, $D = 160 \mu\text{m}$, and chiral V-shaped obstacle design.

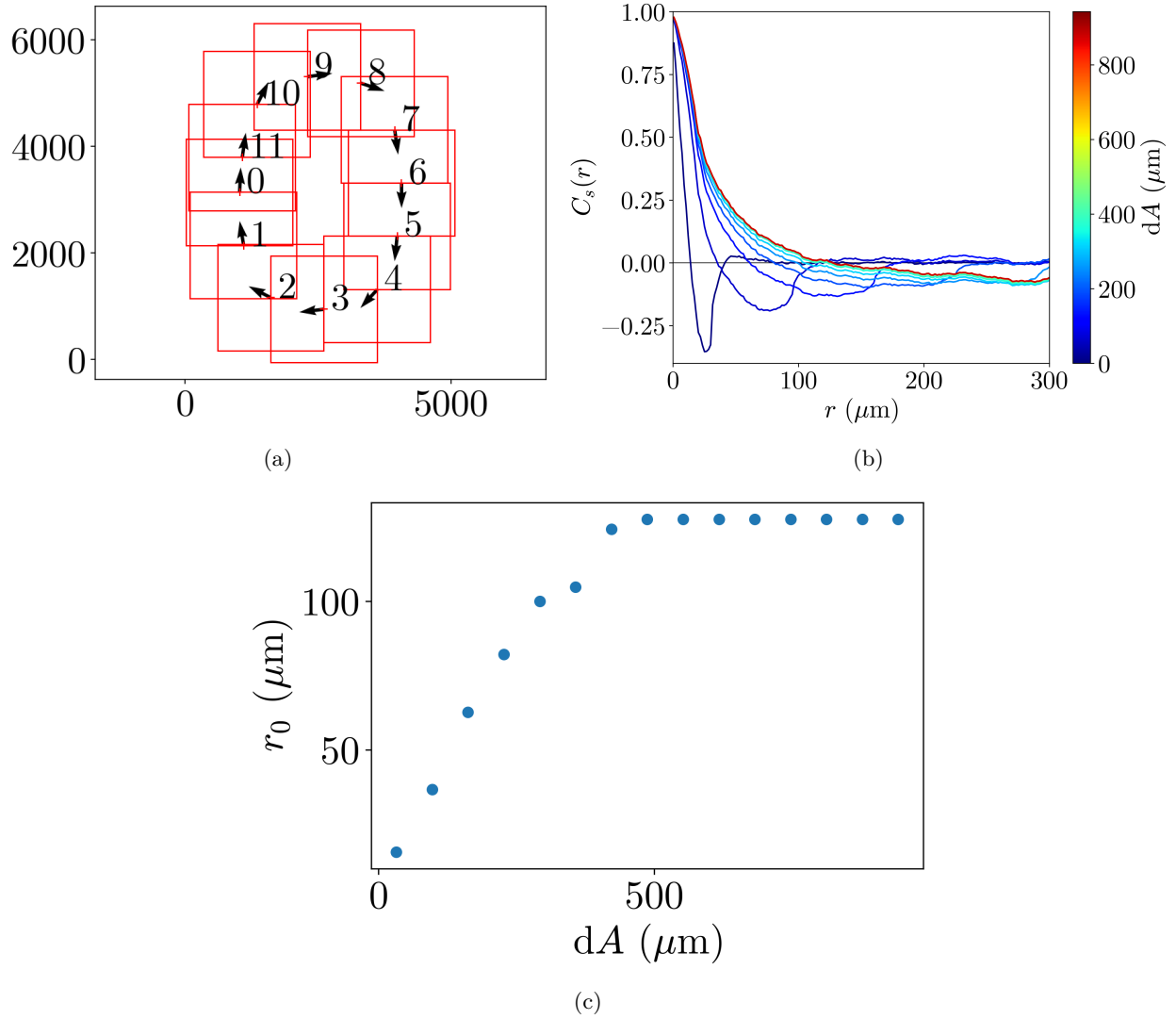


Figure S4: Averaging windows in a racetrack. (a) Division of the racetrack into interrogation windows, here of size $dA = 1300 \mu\text{m}$. Graduations in μm . (b) Autocorrelation function for different values of averaging window size dA , color coded (μm). (c) r_0 values obtained from each curve in (b) vs dA .

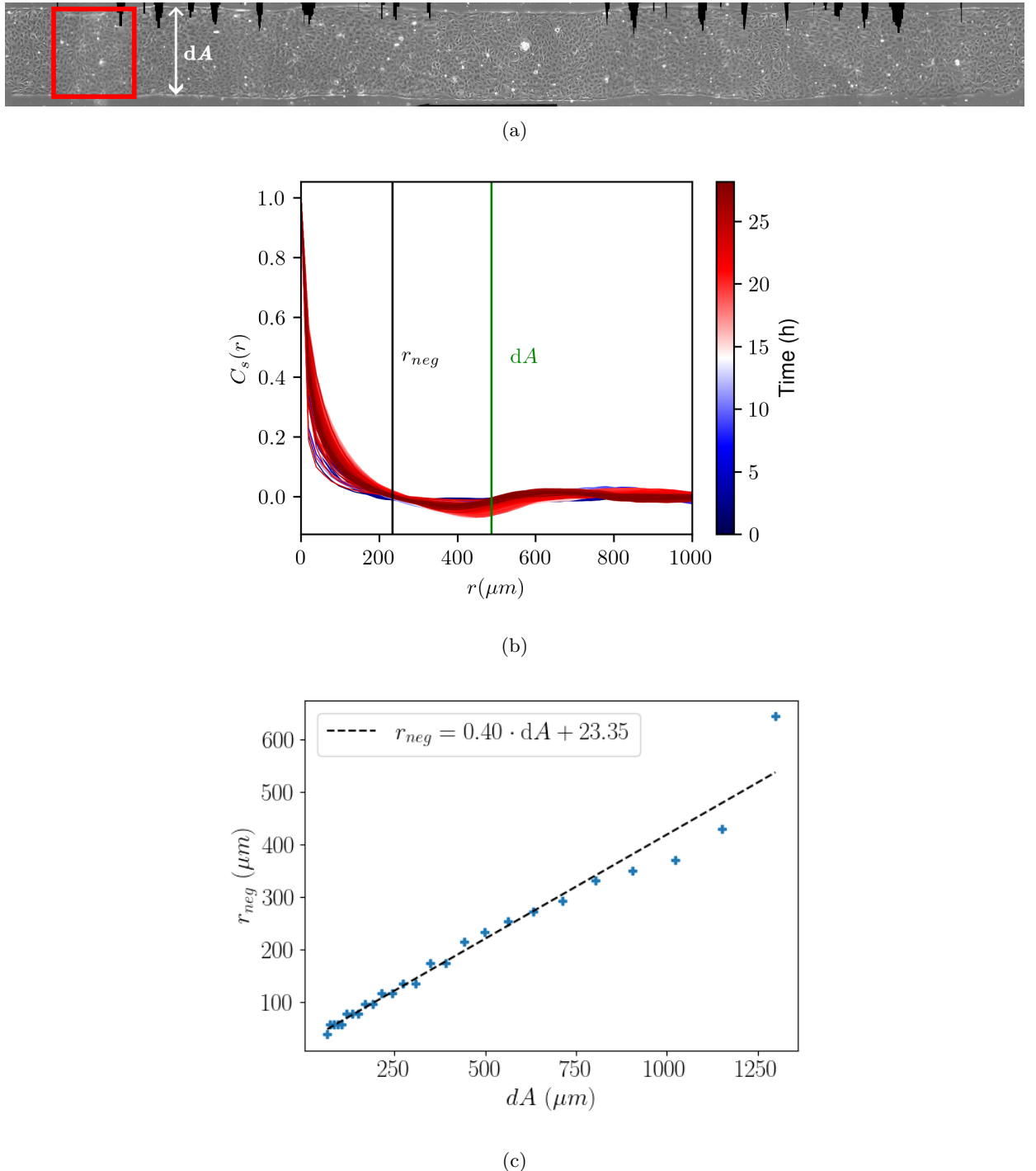


Figure S5: Effect of averaging window size in a racetrack. (a) Transformation of the racetrack images into the curvilinear system of coordinates, with periodic boundary conditions on the right and left sides. In this case, length $L = 6800 \mu\text{m}$, width $W = 600 \mu\text{m}$. (b) Spatial correlation function of the velocity field fluctuations around the spatial average; dA is the average window size (vertical green line). Color code: time (h). Black vertical line: first negative value of the correlation function, r_{neg} . (c) Increase of r_{neg} with the average window size dA . The dashed line is a linear fit to the data.

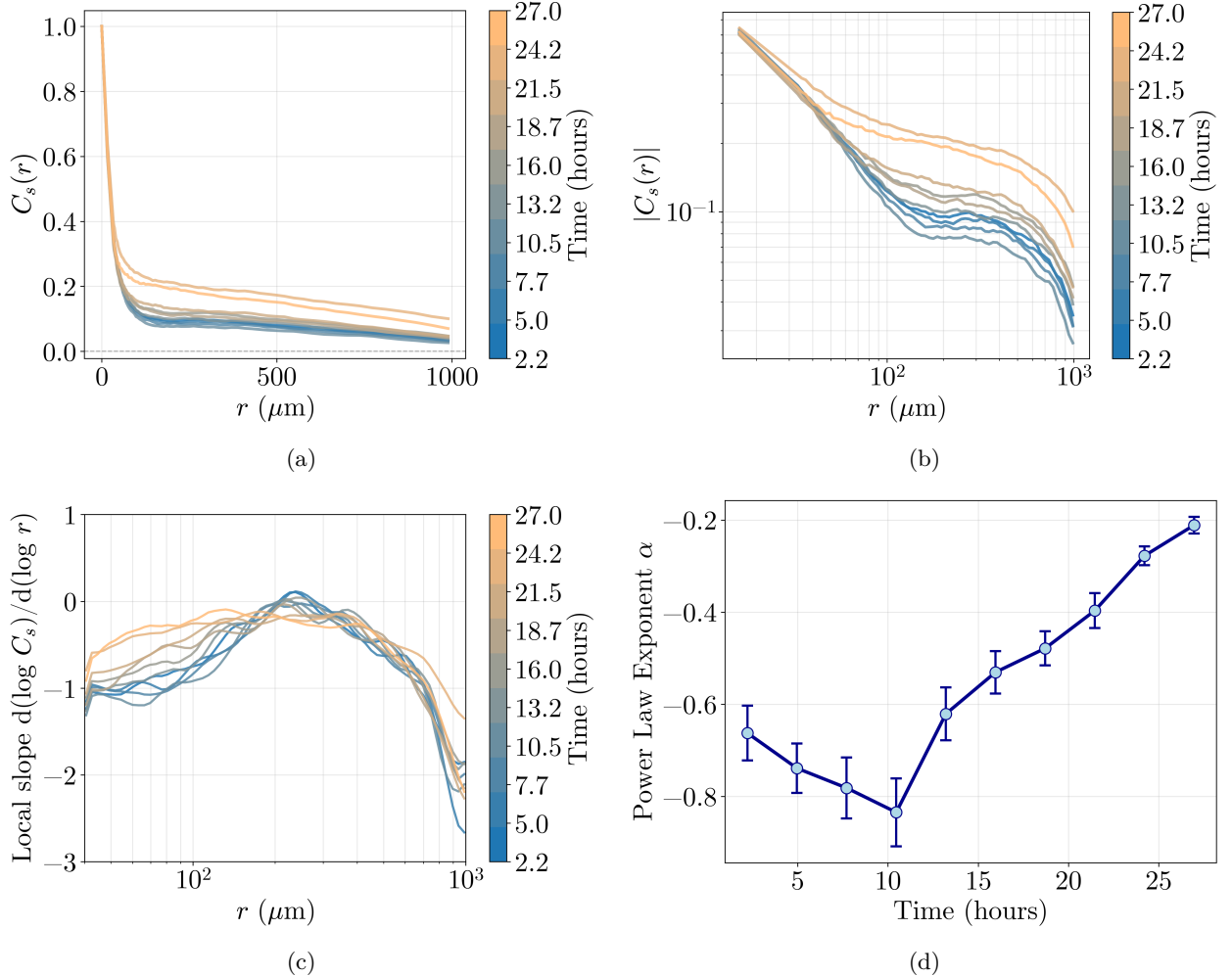


Figure S6: Temporal evolution of the velocity correlation function. Same as Fig. 10 on a racetrack with width $W = 1000 \mu\text{m}$. (a) Spatial correlation function of the velocity versus distance r , for successive times color-coded from 2.2 to 27 h. (b) Same as (a) in log-log scale. (c) Local exponent defined as the slope of (b), i.e. logarithmic derivative of (a). (d) Time evolution of exponent α , defined as the slope in (c), average (\pm s.e.m.) between $r = 30$ and $200 \mu\text{m}$.

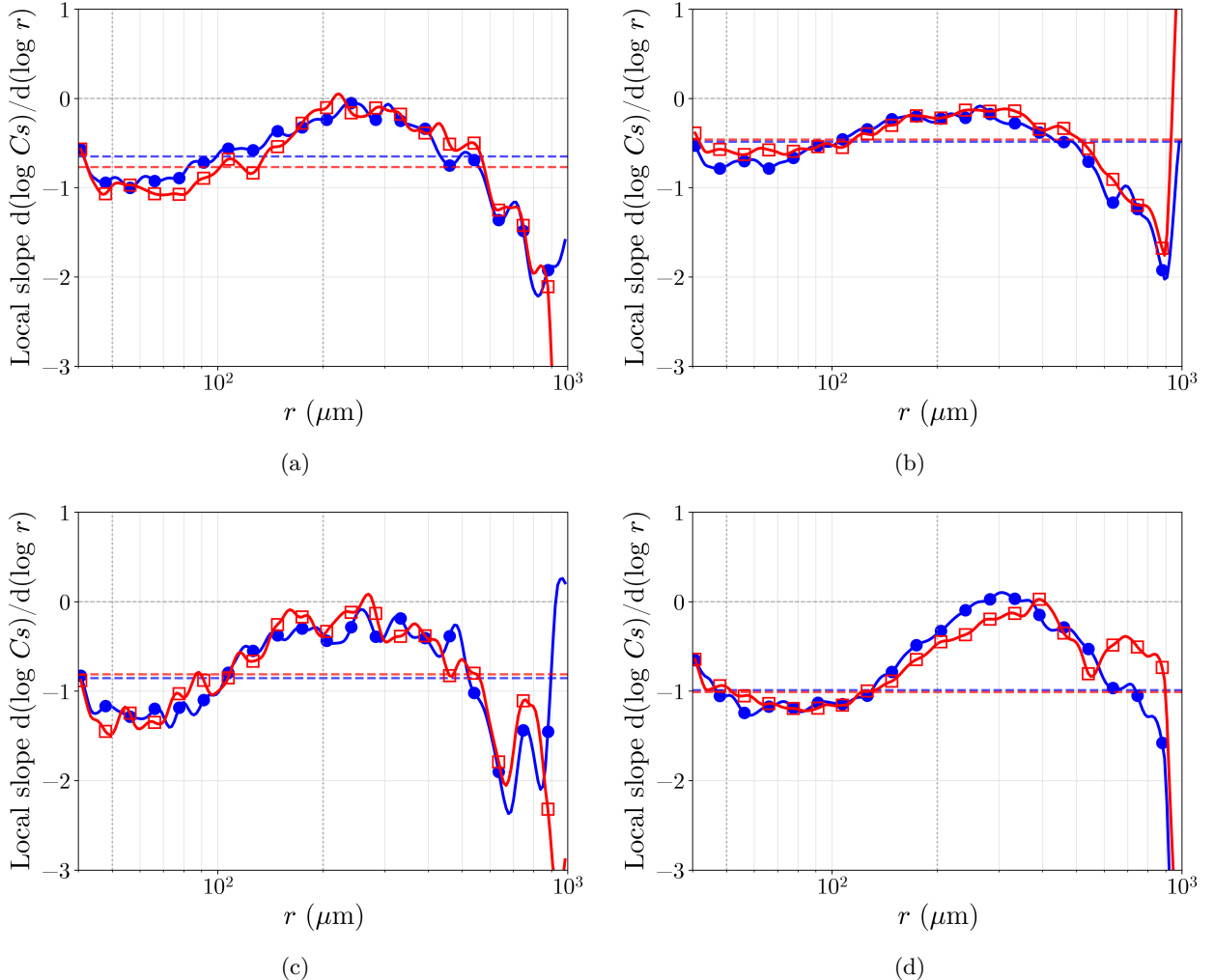
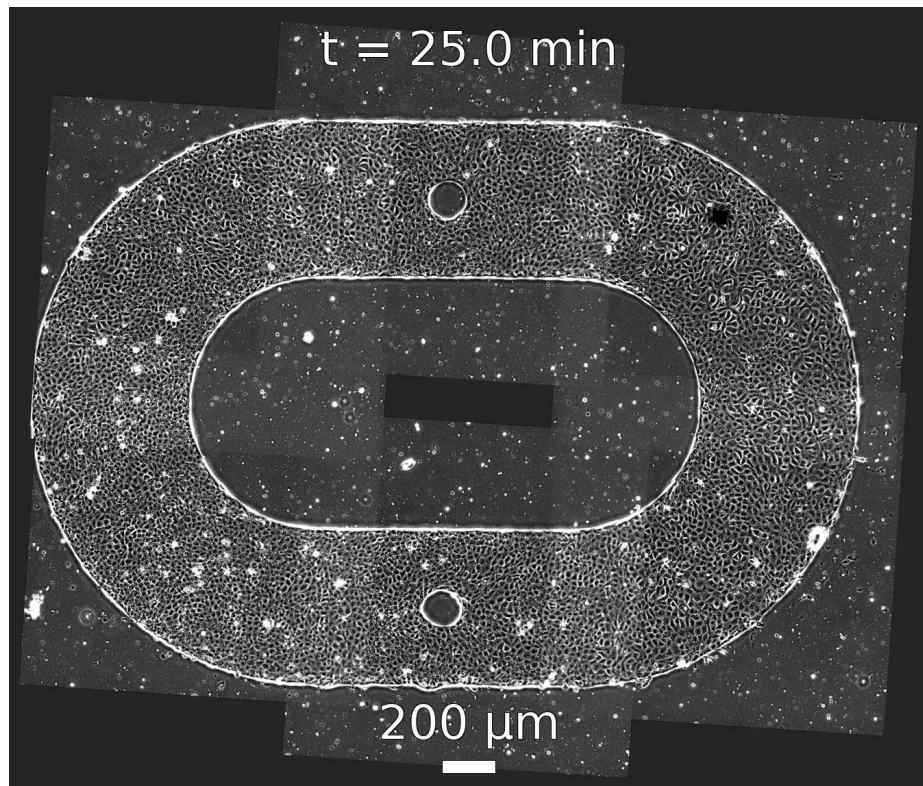
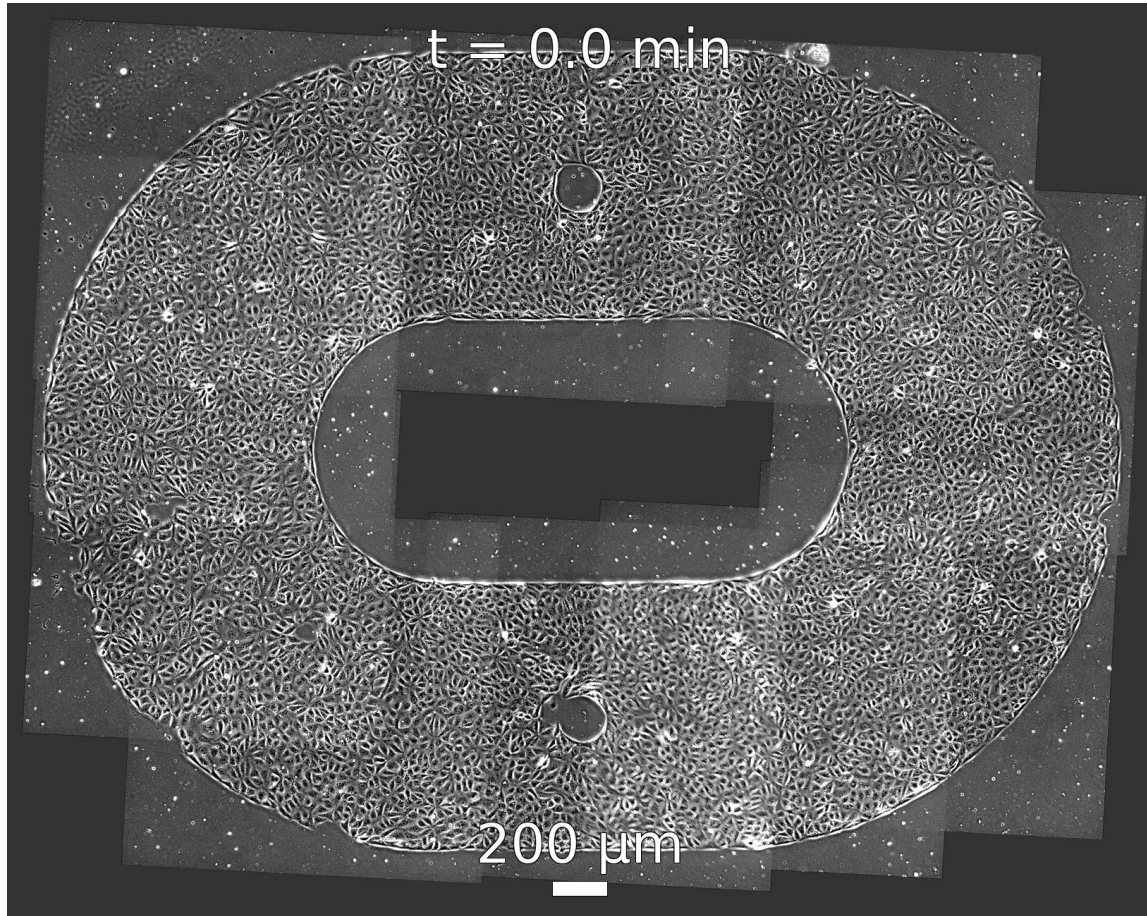


Figure S7: Effects of drugs on the spatial correlation exponents. (a) Control, the medium of the well was renewed but without drug: average exponent -0.65 ± 0.03 before this intervention, -0.77 ± 0.03 after it. (b) CK666 was added to the medium: -0.49 ± 0.02 before, -0.46 ± 0.02 after. (c) Nocodazole was added to the medium: -0.86 ± 0.05 before, -0.81 ± 0.05 after. (d) Simvastatin was added to the medium: -0.99 ± 0.03 before, -1.01 ± 0.02 after. Blue circles before, red squares after.

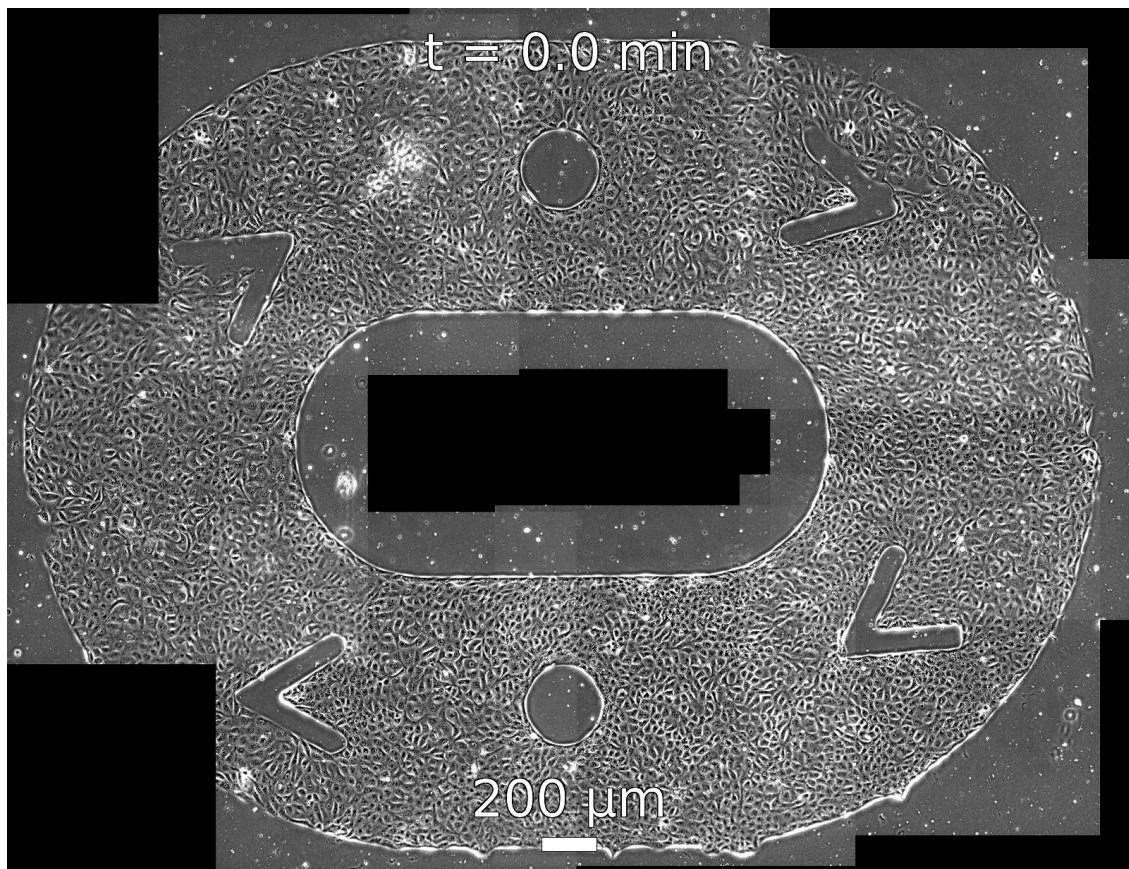
S3 Supplementary Movies



Supplementary Movie 1. Example of racetrack experiment. Track width $W = 600 \mu\text{m}$, obstacle diameter $D = 160 \mu\text{m}$. Interframe 5 min. At the end of the experiment, a drug is added: Simvastatin.



Supplementary Movie 2. Other example of racetrack experiment, with different dimensions. Track width $W = 1000 \mu\text{m}$, obstacle diameter $D = 160 \mu\text{m}$. At the end of the experiment, CK666 is added.



Supplementary Movie 3. Other example of racetrack experiment, with chiral V-shaped obstacle design. Track width $W = 1000 \mu\text{m}$, obstacle diameter $D = 300 \mu\text{m}$. Image with a posteriori linear contrast adjustment. At the end of the experiment, Nocodazole is added.